ALLOY ANODE MATERIALS FOR SODIUM-ION BATTERIES

by

Leah Ellis

Submitted in partial fulfilment of the requirements
for the degree of Master of Science

at

Dalhousie University
Halifax, Nova Scotia
March 2013

DALHOUSIE UNIVERSITY

DEPARTMENT OF CHEMISTRY

The undersigned hereby certify that they have read and recommend to the Faculty of Graduate Studies for acceptance a thesis entitled "Alloy Anode Materials for Sodium-Ion Batteries" by Leah Ellis in partial fulfilment of the requirements for the degree of Master of Science.

Dated: March 27th 2013

Supervisor: _____

Readers: _____

_____

_____

Departmental Representative: _____

DALHOUSIE UNIVERSITY

DATE: March 27th 2013

AUTHOR: Leah Ellis

TITLE: Alloy Anode Materials for Sodium-Ion Batteries

DEPARTMENT OR SCHOOL: Department of Chemistry

DEGREE: M.Sc. CONVOCATION: May YEAR: 2013

_____

Signature of Author

TABLE OF CONTENTS

LIST OF TABLES

LIST OF FIGURES

ABSTRACT

Sodium-ion batteries could one day be an inexpensive alternative to lithium-ion batteries. Many challenges need to be overcome before commercialization of a sodium-ion battery can take place. One of these challenges is the development of an energy dense anode material with good cycle life. This work explores the electrochemical and structural properties of candidate alloy anode materials. After a method was developed for the construction of sodium half-cells, sodium insertion in silicon, tin, lead and bismuth was tested by in-situ x-ray diffraction. An active/inactive nanocomposite of tin was made to optimise the cycle life of tin anodes.

LIST OF ABBREVIATIONS USED

a: fraction of tin accessable for sodiation at a given temperature

a_1, a_2 and a_3: lattice vectors

AHVIC: Annomalous High Voltage Irreversible Capacity

a_i, b_i and c_i: empirical constants

BMF: Blown Microfiber Separator

CCCV: Constant Current Constant Voltage

d: atomic plane spacing

DEC: Diethyl Carbonate

DFT: Density Functional Theory

$D_w(hkl)$: Debye-Waller factor

E: cell potential

e: electron charge

EC: Ethylene Carbonate

$F(hkl)$: Geometric structure factor

$fi(\theta)$: atomic scattering factor

FWHM: Full Width at Half Maximum

$I(\theta)$: total reflected intensity

I_0 : initial intensity

ICSD: Inorganic Crystal Structure Database

K: a constant in the Scherrer equation

$L(\theta)$: Lorentz factor

L: average crystallite size

LPF: Lorenz-polarization Factor

$M(hkl)$: multiplicity

n: number of electrons

NMP: N-Methyl-2-Pyrrolidone

$P(\theta)$: polarization factor

PVDF: Polyvinylidene Fluoride

SEI: Solid Electrolyte Interface

XRD: X-Ray Diffraction

θ: Bragg angle

λ: wavelength

μ: chemical potential

ACKNOWLEDGEMENTS

First I would like to thank Dr. Obrovac for giving me support, guidance and encouragement over the past two and a half years. You've shown me more patenice than I deserve at times when I am nothing but a soggy chicken syrup waffle.

I would like to thank Dr. Jeff Dahn for his help with many things related to this project, and for important discussions and suggestions that greatly improved the scope of this thesis. Dr. Jeff Dahn has taught me many things, the most significant being the value of time and the importance of not wasting it.

I would like to thank Dr. Timothy David Hatchard for being incredibly kind and supportive of me. Tim has always been willing (although perhaps not eager) to help me through every kind of problem. Tim has also taught me many things, such as not to be afraid of empty gas cylinders. Tim is a gem and I will miss him a lot when I leave.

Finally I would like to thank all my coworkers in the Obrovac and Dahn labs, especially Ryan and Tuan who have put up with my shenanigans the longest. Not enough can be said about how creative, kind and intelligent (albeit eccentric) my labmates are. I've had the best time working and making friends with everyone in both these labs.

CHAPTER1 INTRODUCTION

Lithium-ion batteries are the most widely used type of rechargeable battery in the world. Lithium-ion batteries offer significant advantages over previous battery chemistries, such as high energy density (~600 Wh/L) and long cycle life (>1000 cycles) [1]. Since their introduction to the market in the early 1990's, lithium-ion batteries have revolutionized portable electronics, enabling them to become smaller in size, last longer and store more charge. Lithium-ion batteries are now being used to power all-electric vehicles, such as the Tesla Model S™, which rival gasoline powered cars in speed and acceleration [2].

Lithium-ion batteries are comprised of a cathode and an anode, which are separated internally by a porous separator and electrolyte, as shown in Figure 1.1. The cathode is typically a lithium transition metal oxide, such as $LiCoO_2$, while the anode is typically graphite. When the cell is being discharged, the anode loses an electron and a Li^+ ion simultaneously enters the electrolyte. The electron travels through the external circuit and does work (powers your portable device). The electron arrives at the cathode while simultaneously a Li^+ ion is accepted into the cathode from the electrolyte. This results in the lowering of oxidation state of a transition metal in the cathode.

Unlike previous rechargeable battery chemistries, lithium-ion batteries operate by what is commonly called the "rocking chair" mechanism. Both the anode and cathode materials of a lithium-ion battery can host lithium ions, usually via intercalation. Intercalation occurs when guest atoms (in this case lithium) can be reversibly inserted

into host materials without significant deformation of the host structure. The shuttling back and forth of the active ions during charge and discharge is what gives rise to the term “rocking chair model”. This is the operating principle on which all metal-ion battery chemistries are based, including sodium-ion batteries, which are the topic of this work.

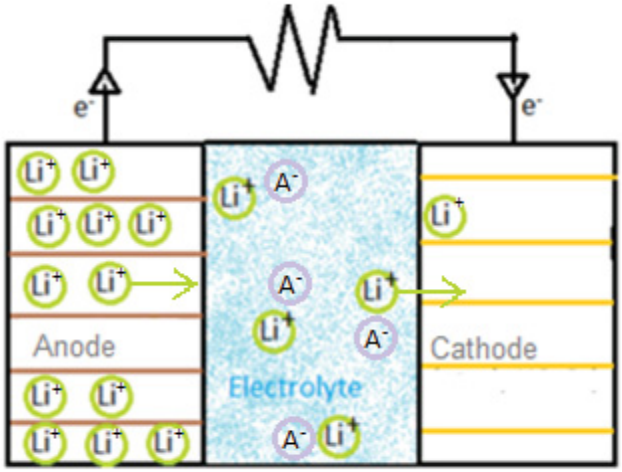

Figure 1.1: A lithium-ion battery being discharged.

Sodium-ion batteries are particularly interesting as an alternate metal-ion battery chemistry because of the chemical similarity between sodium and lithium metals. During the 1980's when ambient temperature lithium batteries were first being proposed , sodium batteries were also considered as possible high energy density battery chemistries [3-10]. Research in lithium-ion chemistries resulted in their mass commercialization, while sodium-ion batteries were never fully developed. In the past few years interest in sodium-ion batteries has been renewed, inspired in part by the success of lithium-ion batteries, and also by the possibility of using inexpensive and sustainable materials.

Recently it has been shown that Ni/Mn-based cathodes can achieve similar volumetric energy densities as $LiNi_{0.33}Mn_{00.33}Co_{0.33}O_2$, a high energy density cathode material used in most Li-ion cells [11]. The ability to reach such high capacities with inexpensive transition metals is significant, since lithium-ion cathodes are most often based on cobalt, which is very costly. Should sodium-ion batteries be commercialized using cathodes based on inexpensive transition metals, the environmental and cost savings will be significant. It has also been shown that some sodium-ion cathodes are highly thermally stable because little oxygen, which combusts with electrolyte at high temperature, is released upon heating [12]. Additionally, sodium does not alloy with aluminium, which would allow aluminium to replace copper in the anode current collector, leading to a further cost advantage.

Despite many achievements in recent years, the advancement of sodium-ion batteries still faces many challenges. The development of a practical anode material is the greatest of these challenges. Graphite is the most commonly used anode material for lithium-ion batteries. It has a capacity of 372 mAh/g, or 750 mAh/cm^3, with only 12% volume expansion at full lithiation. Graphite can be compressed (calendered) into very dense electrode coatings, which can withstand many cycles without damage, due to low volume expansion. Sodium, however, does not intercalate in graphite to a significant degree [13], challenging researchers to find a suitable replacement for a sodium-ion anode.

Other carbon morphologies have been proposed for sodium storage at the anode, most notably hard carbon [14]. Hard carbon is composed of randomly oriented graphitic crystallites, which form a disordered, porous, non-graphitizable structure [15]. Hard

carbon can be made from many different aliphatic organic precursors by heating in inert atmosphere to temperatures above 700°C [15]. The structure of hard carbon obtained by heat treatment can be described by the "Falling Cards" model [15]. In this model graphitic regions are seen as "cards" which are stacked randomly against each other to form pores, similar to a house of cards, as seen in Figure 1.2. As hard carbon is heated, the graphite sheets, or "cards", rotate and fall parallel to each other , increasing the pore size in the material. Hard carbon is non-graphitizable, and is therefore not able to entirely resolve its disordered structure upon heating [15].

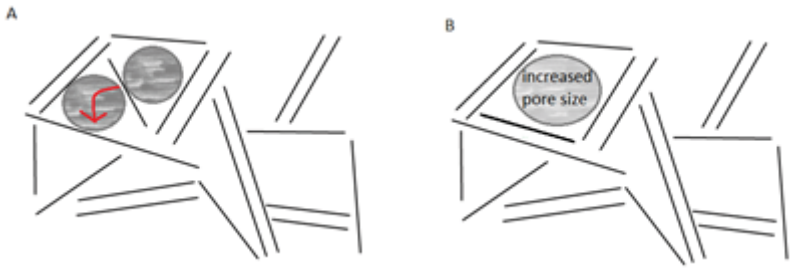

Figure 1.2: "Falling Cards" model of hard carbon, a) unheated, b) heated

Lithium and sodium can be accommodated by hard carbon in two ways: adsorption within pores, and intercalation in the graphitic regions, as illustrated in Figure 1.3 [14]. Through these mechanisms, hard carbon heat treated to 1100°C has a lithium capacity of 560 mAh/g and a sodium capacity of 300 mAh/g [14].

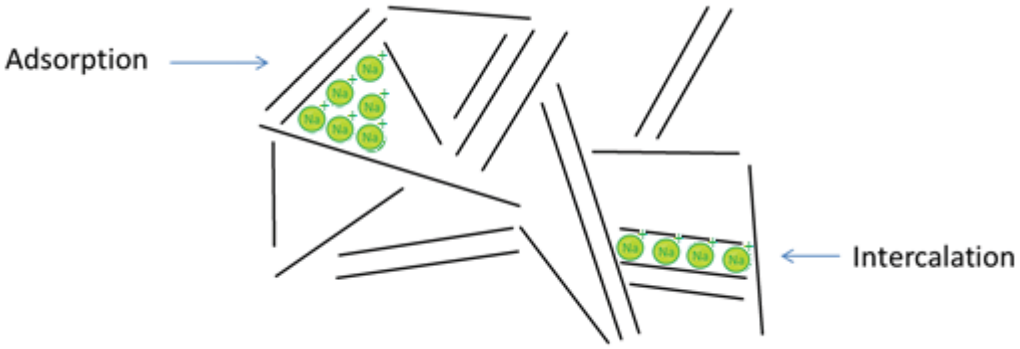

Figure 1.3: Hard carbon with sodium adsorption and intercalation

Compared to the theoretical gravimetric capacity of graphite in lithium cells, 372 mAh/g, the sodiation capacity of hard carbon is reasonably high. However, due to hard carbon's low density of 2.11 g/cm^3 [16], it has a low volumetric capacity of 630 mAh/cm^3, compared to 750 mAh/cm^3 for lithium in graphite. Although gravimetric capacity is an important factor in the practical use of an electrode material, especially in large cells, volumetric capacity is often more important, as in consumer electronics.

Alloys are anticipated to be the next-generation anode materials in lithium-ion cells due to their high volumetric capacities. Silicon, for example, can be lithiated to a maximum of $Li_{15}Si_4$, which corresponds to 3580 mAh/g and 2189 mAh/cm^3 at full lithiation [17]. Transitioning from graphitic anodes to alloy anodes is expected to dramatically increase the capacity and energy density of lithium-ion batteries in the coming years. Already, anode materials based on silicon are being marketed with the claim that they can increase the energy density of commercial cells by more than 20% when paired with a high energy density cathode and an optimised cell design [18].

Because of their high volume expansion upon lithiation, the implementation of lithium alloy negative electrodes is difficult. The lithiation of silicon to $Li_{15}Si_4$ causes an increase in volume of 281%, which is difficult to accommodate in a commercial cell. The electrode material experiences considerable mechanical stress with large and repeated changes in volume. Eventually the alloy particles can be pulverized with repeated cycling, leaving fragments that are electrically isolated from the current collector. This can lead to significant capacity fade [19].

Researchers have developed a number of ways to overcome these issues. One way is to reduce the amount of active material in the alloy so that the alloy particle expansion is reduced to about 100%. In such alloys the active phase is combined with an inactive component, making an active-inactive composite [20]. In order to prevent electrode fracturing due to volume changes, various conductive polymeric binders have been developed which bind strongly to alloy particles, keeping them in electrical contact with the current collector [21, 22]. Decreasing the size of active particles also reduces fracturing and improves cycling by decreasing the mechanical stress experienced by the particle during cycling. Nanosized and amorphous particles expand homogeneously, while crystalline materials undergo structural transitions to phases with different lattice constants, leading to inhomogeneous expansion [23]. Active/inactive composites are usually made to be amorphous or nanostructured to avoid phase transitions which cause complicated structural rearrangements on the atomic level and electrode degradation [19,20].

Alloys are also expected to improve the volumetric capacity of sodium-ion anodes [24], which as of yet have not exceeded 630 mAh/cm^3 from hard carbon. A number of earth abundant metals are predicted to form binary alloys with sodium, including silicon, tin, lead, bismuth and antimony [25]. Alloy anodes made from these materials would have volumetric capacities upward of 900 mAh/cm^3, and would help to narrow the gap between the volumetric capacities of lithium and sodium-ion technologies.

This thesis will explore the use of metals as anodes in sodium-ion batteries, with the hope of increasing the volumetric capacity of the sodium-ion anode. After a theoretical background of the methods used, experiments are described in which sodium electrochemical half-cells were developed as a test vehicle for this and future sodium-ion materials research. This cell design was then used to evaluate sodium insertion into silicon, tin, lead, and bismuth metals. Finally, the use of active/inactive materials is explored for their potential use as practical anode materials in sodium-ion cells.

CHAPTER 2 EXPERIMENTAL METHODS

2.1 X-RAY DIFFRACTION THEORY

X-radiation has a wavelength between 0.01 and 10 nm, (flanked by ultraviolet light and gamma rays in the electromagnetic spectrum). X-radiation was first observed and produced by Wilhelm Röntgen in 1895. X-rays are most commonly created in a vacuum tube by the interaction of high energy electrons with a heavy metal target. When electrons strike an atom in the metal target they can knock an electron out of a core shell. An electron from a higher energy level drops down to fill the vacancy, releasing an x-ray with a sharply defined energy equal to the difference between the initial and final energy states of the electron. Such x-rays are known as characteristic x-rays. A common type of x-radiation used for crystallography is copper Kα radiation, which is emitted when the impact of an incident high-energy electron ejects an electron out of the electron shell closest to copper's nucleus (known as the 1s or K shell), leaving a vacancy which is quickly filled by an electron from the second closest shell from the nucleus (the 2p or L shell).

Due to spin-orbit coupling, two energy levels exist within the Cu L subshell: $2p_{1/2}$ and $2p_{3/2}$ (or L_2 and L_3), which give rise to transitions of slightly different energy. The Kα1 transition is from the doubly degenerate L_3 ($2p_{3/2}$) to the K (1s) orbital. The difference in energy between these two states is 8.048 keV [26], which corresponds to a photon with a wavelength of 1.541 Å. The Kα2 transition is from the L_2 ($2p_{1/2}$) to the K (1s) energy level, which are 8.028 keV apart, resulting in the emission of a photon with a wavelength of 1.544 Å. The Kα1 radiation has the highest intensity and is therefore the

most desirable from which to conduct XRD. The similarity in their wavelength makes it impossible to separate Kα1 and Kα2 with the right monochromator, which filters out radiation from all other transitions. At low scattering angles, diffraction peaks resulting from Kα1 and Kα2 radiation occur at approximately the same scattering angle. At higher angles, peak splitting can be discerned in accordance with the Bragg equation (Equation 2.11). Due to the double degeneracy of the $2p_{3/2}$ energy level, Kα1 radiation is observed with twice the intensity of Kα2 radiation, making Kα2 peaks at high angles easily identifiable.

Once x-rays leave the x-ray tube, and optionally an incident beam monochromator, they pass through various slits, which control the size of the x-ray beam. The x-rays then strike the powder sample, and are scattered from the electrons in the sample. Because the wavelength of x-radiation is similar in size to interatomic spacings in solids, diffraction patterns can be observed due to constructive and destructive interference of x-rays scattered from an ordered arrangement of atoms. The condition for constructive interference is given by the Bragg Law:

$$n\lambda = 2d \sin\theta. \qquad (2.11)$$

In this relationship, n is an integer corresponding to the order of the reflection, λ is the wavelength of radiation used (1.54 Å for CuKα), and θ is the angle of the incident radiation to the sample. This relationship can be derived by trigonometry, as shown in Figure 2.1.1. When the difference in the distance travelled by adjacent photons is equal to an integer multiple of its wavelength, the photons will be in phase and the amplitudes of their waves will add (constructive interference), resulting in radiation with increased

intensity. When the difference between the distance travelled by adjacent photons equals an integer multiple of half the wavelength, the scattered photons will be opposite in phase, which will result in destructive interference.

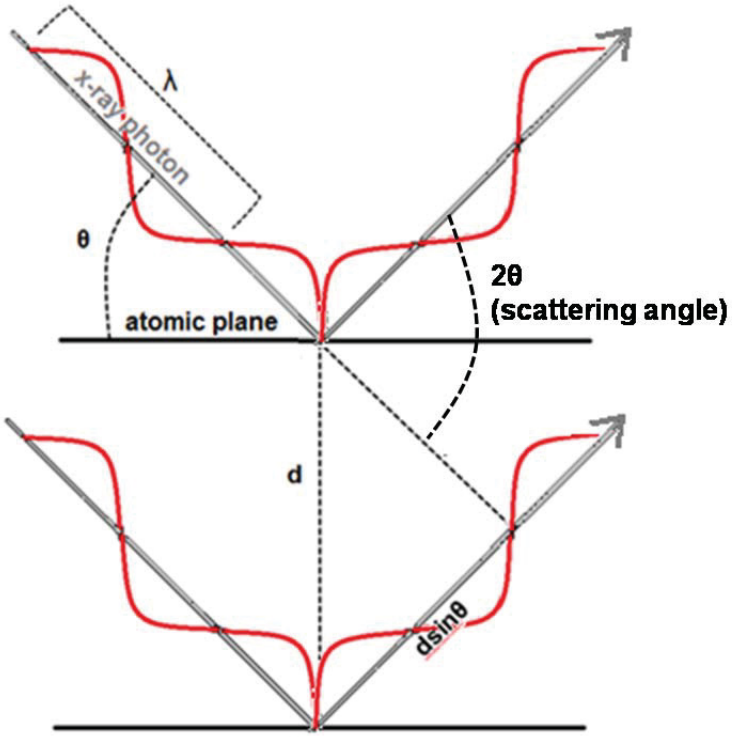

Figure 2.1.1: Bragg scattering from crystalline planes in a solid.

XRD patterns are often plotted as intensity of scattered radiation vs. the scattering angle, 2θ. At values of 2θ which give constructive interference, peaks in the scattered x-ray intensity will be observed. Using the peak positions and the Bragg Law, Equation 2.11, the interplane atomic spacings, *d*, can be calculated.

The use of Miller indices provides a convenient way of describing reflections from atomic planes in a crystal. The Miller indices, *h,k* and *l*, are the reciprocal intercepts of the lattice vectors a_1, a_2 and a_3 which define a unit cell. A Miller index of 0 indicates that the plane described by *hkl* does not intercept the axis of the corresponding lattice vector. The use of Miller indices is demonstrated by Figure 2.1.2, which shows representative planes in a 2H graphite lattice and the XRD pattern of graphite. Each peak is labelled with the Miller index of the crystal plane whose *d* spacing satisfies the Bragg equation at the corresponding scattering angle.

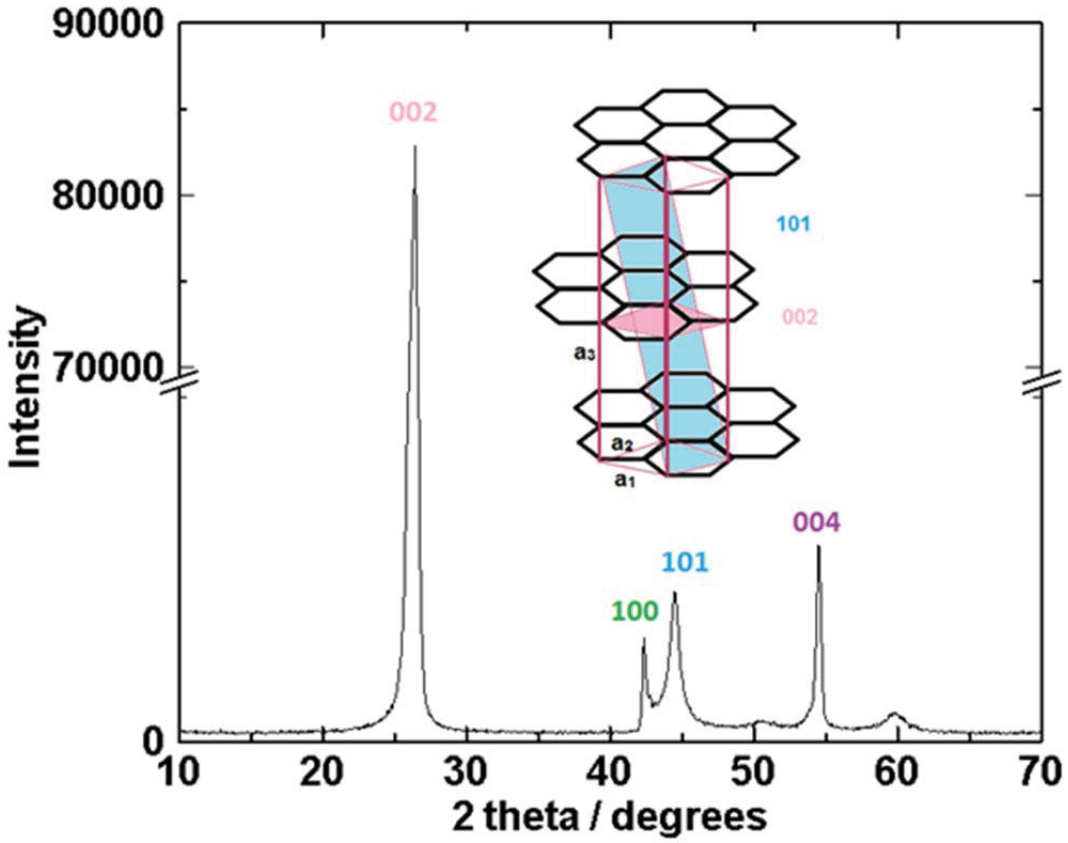

Figure 2.1.2: XRD pattern of graphite. Peaks are labelled with the corresponding Miller indices. **Figure 2.1.2 (inset)** A cartoon showing the structure of 2H graphite with the 101 and 002 planes.

The XRD pattern of graphite in Figure 2.1.2 contains sharp, high intensity peaks, as one would expect from a highly crystalline material. Battery materials may also be amorphous, disordered or nanostructured. Amorphous materials lack long range order, leading to incoherent scattering and broad diffuse peaks corresponding to average atomic arrangements. Disordered or nanostructured materials contain ordered regions which are on the order of 10-1000 times the wavelength of x-radiation. This leads to decreased scattering intensity and peak broadening. Hard carbon, for example, which is discussed in the introduction and whose structure is shown in Figure 1.2, is a disordered carbon with graphitic crystallites. The XRD pattern of hard carbon is shown in Figure 2.1.3. The pattern contains the same peaks that are present in Figure 2.1.2 for crystalline graphite, but with much broader peak widths and lower intensity.

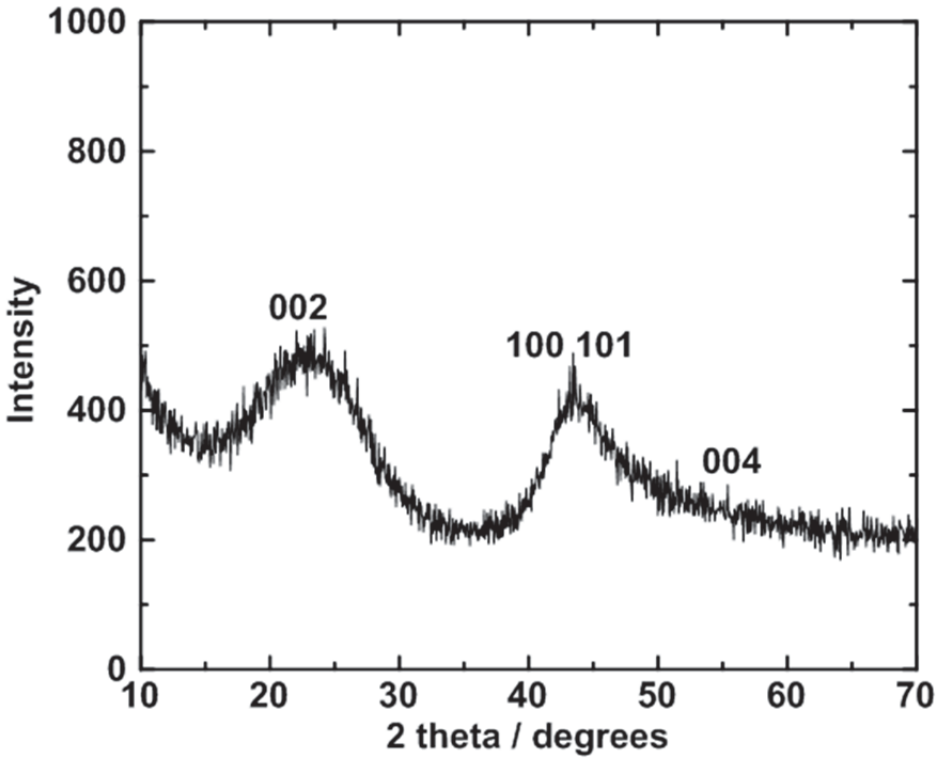

Figure 2.1.3: XRD pattern for hard carbon (synthesis described in Section 3.2).

Peak broadening associated with small crystallite size is described by the Scherrer equation:

$$FWHM = \frac{K\,\lambda}{L\,cos\theta} \qquad (2.1.2)$$

where FWHM is the full width at half maximum of the peak in radians, *K* is a constant (0.9 for the 002 peak of graphite, and 1.84 for the 100 peak [27] and *L* is the average dimension of the crystallites perpendicular to the plane defined by the Miller indices of the peak in Å.

It is important to take into account factors that can cause peak distortion. For instance, the intensity of diffracted x-rays is proportional to the intensity of the incident radiation, I_o, polarization factor, *P(θ);* Lorentz factor, *L(θ)*; geometric structure factor, *F(hkl)*; multiplicity, *M*(*hlk*); and the Debye-Waler factor, $D_w(hkl)$. The total intensity of an XRD peak is given by Equation 2.1.3:

$$I(\theta) = I_0\,P(\theta)\,L(\theta)\,F^2(hkl)\,M(hkl)\;\;D_w(hkl)\;. \qquad (2.1.3)$$

Some of these factors are θ dependent, and, as such, can result in significant distortion of broad peaks from disordered materials. Narrow peaks characteristic of crystalline materials are less affected. XRD patterns from disordered materials must be corrected for these effects in order to obtain accurate values for the average crystallite size using Scherrer Equation 2.1.2 [28].

Of the factors in Equation 2.1.3, the geometric structure factor, *F(hkl)*, the polarization factor, P(θ), and the Lorentz factor, L(θ), cause peak distortion at low angles. The structure factor, *F(hkl)*, contains a geometric sum of the atomic form factors, $f_i(\theta)$, of

the atoms in the unit cell. The atomic form factor modifies the intensity of scattered x-rays from specific atoms as a function of θ, and thus contributes to peak broadening. The atomic form factor contains only one type of atom and can be approximated by Equation 2.1.4 [29]:

$$fi(\theta) = \sum_{i=1}^{4} a_i \exp(b_i (\frac{sin\theta}{\lambda})^2) + c \qquad (2.1.4)$$

where a_i, b_i and c are empirical constants [30]. The contribution of the atomic form factor to the scattered intensity, given by Equation 2.1.3, is plotted in Figure 2.1.4 for carbon and is large at low scattering angles.

The polarization factor, $P(\theta)$, results from the partial polarization of x-radiation by reflection from the crystal and is given by Equation 2.1.5 [31] :

$$P(\theta) = \frac{1+cos^2 2\theta_m cos^2 2\theta}{1+cos^2 2\theta_m} \quad , \qquad (2.1.5)$$

where θ is the Bragg angle at the sample and θ_m is the Bragg angle for the monochromator crystal (13.3° for a graphite crystal).

The Lorentz factor, $L(\theta)$, given by Equation 2.1.6, takes into account the variability of beam area with scattering angle in an apparatus with fixed slits [31]:

. $$L(\theta) = \frac{1}{sin^2 2\theta} \qquad (2.1.6).$$

Since both the polarization factor and the Lorentz factor depend on θ only, they are often computed together as the Lorentz-polarization factor (LPF), given by the product of

Equations 2.1.5 and 2.1.6. At low angles, the contribution of the LPF to the diffracted intensity is very high, as shown in Figure 2.1.4.

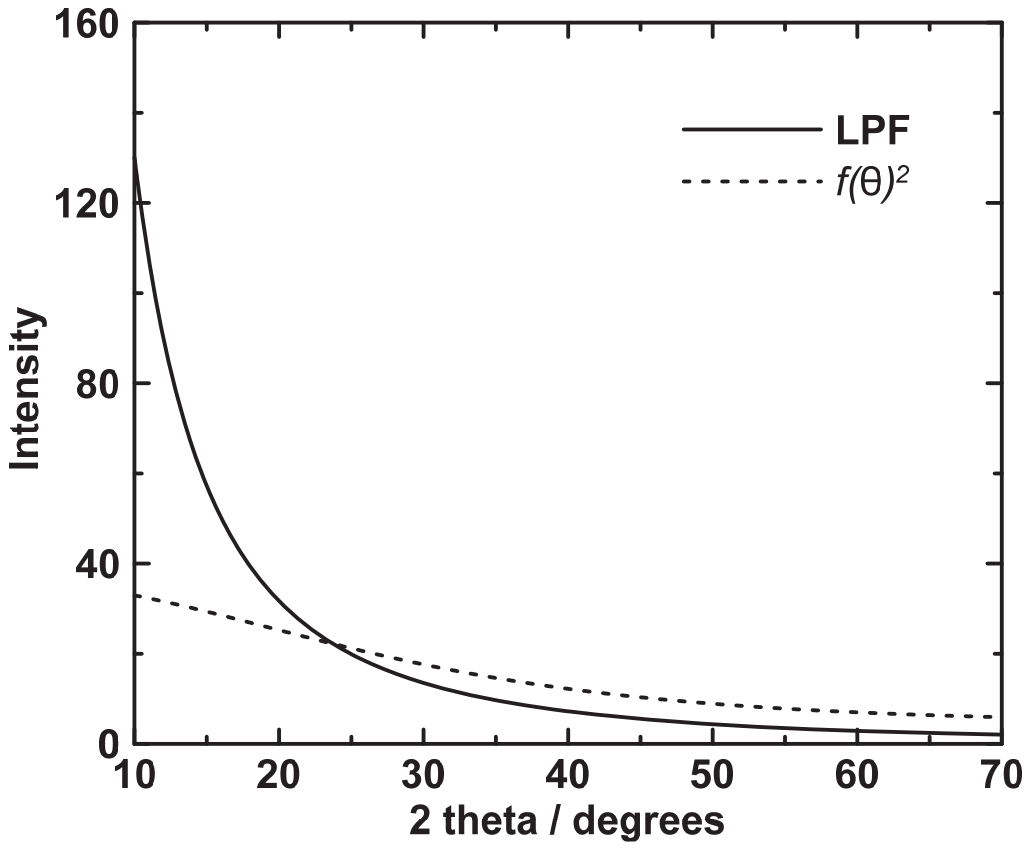

Figure 2.1.4: The intensities due to the atomic scattering factor, *f(θ)*, and the Lorentz-polarazation factor, LPF.

In order to remove distortions at low angles, the x-ray pattern must be divided by $P(\theta)\,L(\theta)\,F^2(hkl)$, in accordance with Equation 2.1.3. Figure 2.1.5 shows the XRD pattern of hard carbon prepared at 1100°C from glucose before and after LPF and atomic form factor correction. Significant distortion, especially of the 002 peak, by the structure factor and LPF effects is readily apparent and results in a peak shift to low angles.

Applying the LPF and atomic form factor correction allows for accurate analysis of the XRD pattern for plane spacings and crystallite size.

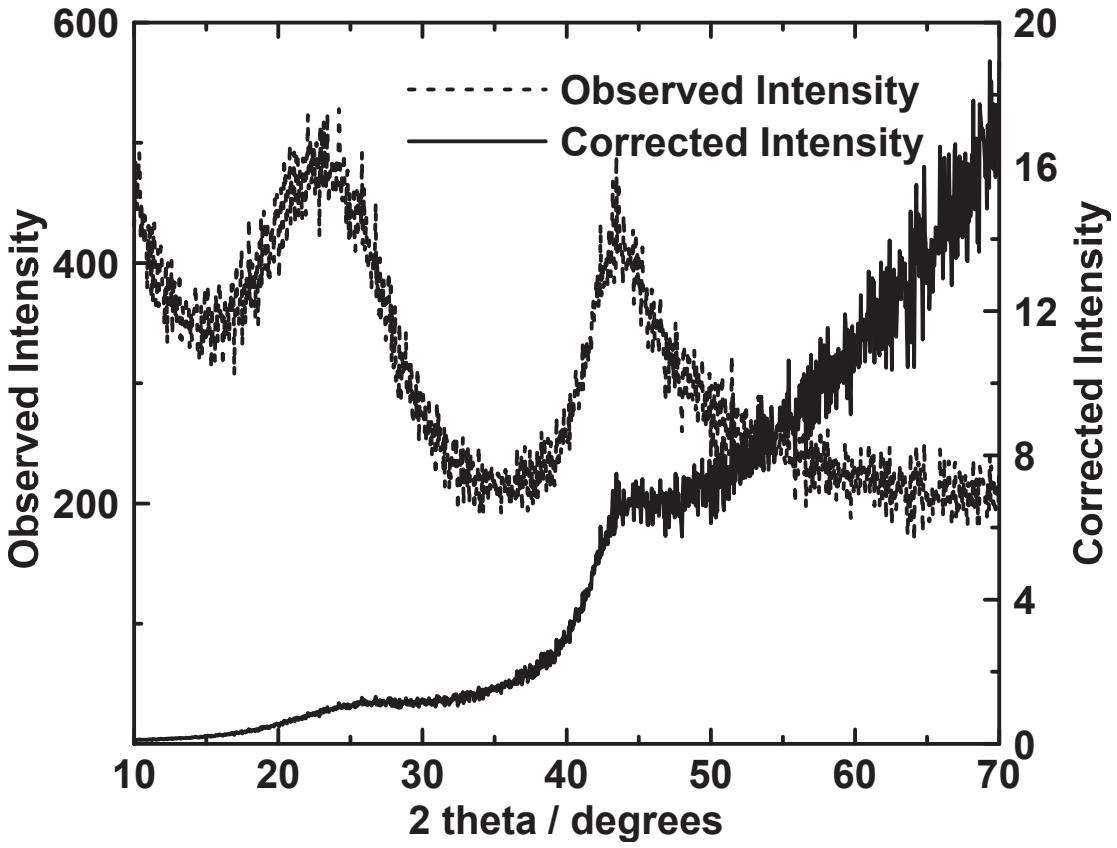

Figure 2.1.5: The XRD pattern of hard carbon, before and after LPF and atomic form factor correction.

To extract precise structural information, including lattice constants, atom positions and site occupations, XRD pattern can be fit to calculated powder patterns based on trial crystal structures in a process known as Rietveld refinement. Rietveld refinements can be performed using various software programs, such as Rietica and Powdercell, which are available for free online.

2.2 Electrochemical Methods

Electrochemical techniques were used to evaluate the performance of candidate electrode materials. Relevant factors in an electrode material's commercial eligibility can be measured electrochemically, including its operational voltage range, capacity (amount of charged stored), energy density, rate capability and cycle life. Phase changes, and diffusion behaviour can also be interpreted from appropriate electrochemical measurements. In this thesis CCCV (Constant Current, Constant Voltage) measurements, which mimic the cycling protocol of commercial lithium-ion cells, were performed on all candidate anode materials. This section will discuss the thermodynamics behind the electrochemical response of battery materials, and explain how useful parameters can be obtained from electrochemical measurements.

A metal-ion electrochemical cell, as described in the introduction and illustrated by Figure 1.1, consists of an anode and a cathode, separated by an electrically insulating separator soaked in electrolyte, and connected by an external circuit. The cell potential of a metal ion cell in volts is given by Equation 2.2.1:

$$E = \frac{-(\mu_{cathode} - \mu_{anode})}{ne}, \qquad (2.2.1)$$

where $\mu_{cathode}$ and μ_{anode} are the chemical potentials of the metal ion in the cathode and anode, respectively, n is the number of active electrons per metal ion and e is the electronic charge [1]. In the case of sodium or lithium $n = 1$. By definition, the cathode is the electrode at which reduction occurs and the anode is the electrode at which oxidation occurs during cell discharge. All electrochemical measurments in this thesis

were conducted using half-cells, in which working electrodes comprising materials of interest are cycled versus a sodium metal reference/counter electrode.

Since the chemical potential of the sodium reference electrode does not change with the cell's state of charge, Equation 2.2.1 can be simplified to Equation 2.2.2 for a monovalent metal-ion half-cell:

$$Voltage\ versus\ reference\ electrode\ = \frac{-(\mu_{working\ electrode})}{e}. \qquad (2.2.2)$$

As long as the impedance on the reference electrode is small, the changes in measured voltage in a half-cell, to a good approximation, occur only from changes in the chemical potential of the working electrode. This allows properties, such as capacity and chemical potential of intercalation sites, of single electrodes to be measured.

Typically, a material's gravimetric capacity is measured in units of mAh/g in the battery community, although the proper SI units of gravimetric capacity are C/g. Volumetric capacities are measured in mAh/cm^3 or Ah/L. Cycling currents are normally expressed as a 'C-rate', which is the capacity of the cell in mAh divided by the number of hours desired to complete a half-cycle. A rate of C/10, for example, would be a current a tenth of the magnitude of a material's full capacity, and would result in each charge or discharge half-cycle nominally lasting 10 hours.

In most devices lithium-ion cells are charged using a CCCV charging protocol. In order to replicate this, half-cells are first discharged at a constant current (CC). The potential of the cell decreases as the cell is being discharged until the desired lower cut off potential is reached. The voltage is the held at the lower cut off potential until the

current decays to a lower cut-off current limit (this is the CV step), which allows the system to come to equilibrium. After this step is complete, the cells are charged at the same constant current to a suitable upper potential limit, thus completing a full cycle.

The most common method to display cycling data is a voltage curve, in which the measured voltage is plotted versus the working electrode's accumulated gravimetric capacity. The features in a voltage curve correspond to changes in the chemical potential of the metal ions in the host electrode.

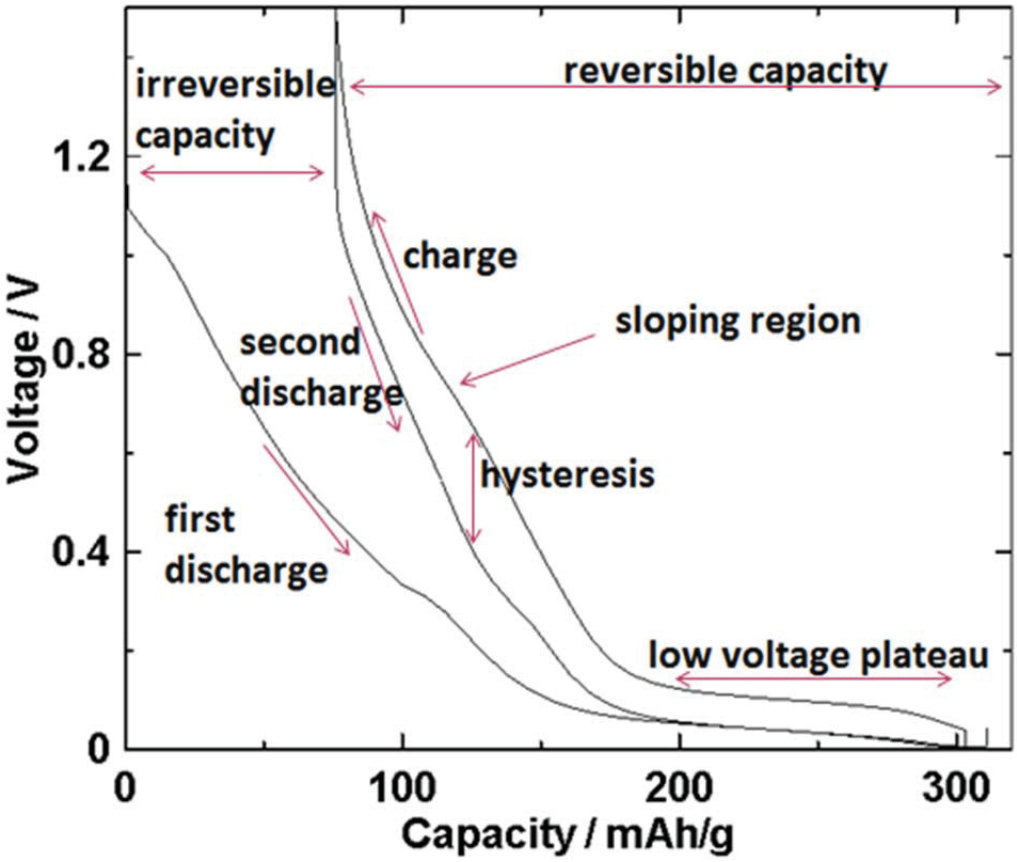

Figure 2.2.1: The voltage curve of a sodium-hard carbon half-cell.

In the voltage curve of hard carbon vs. sodium, shown in Figure 2.2.1, the sloping region of the voltage curve is due to insertion of sodium between graphitic sheets, and the low voltage plateau is due to clustering of sodium within the pores of the hard carbon [14]. Plateaus in voltage curves typically occur when two-phase regions are encountered in the active metal / host electrode phase system (only one degree of freedom exists in the system at constant temperature). Sloping regions in the voltage curve are typically indicative of single-phase regions.

Charge transfer kinetics, ion diffusion through the electrolyte or electrode, and the electrical resistance of the cell parts cause polarization of the cell voltage during cycling. This manifests itself as a difference between the average voltage of the charge and discharge curves. When current supplied to the cell is stopped for a sufficient period of time, the measured voltage eventually recovers from polarization and returns to the open circuit voltage, or the thermodynamic potential at that point of charge. Structural changes that occur during cycling, such as phase transitions in alloy materials, can be path dependent, and can cause hysteresis between the charge and discharge curves.

Electrochemical cells in this work were made in 2325 type coin cells. Coin cells are made by stacking the electrodes and separator with excess electrolyte in a stainless steel can. A spacer and a conical spring washer are added to apply an appropriate pressure on the electrodes and ensure good electrical contact. The bottom and top halves of the coin cell can are separated by a plastic gasket, to prevent electrical contact, and the cell is crimped shut. Figure 2.2.2 shows a general schematic of a lithium coin cell assembly. Sodium half-cells made in this way did not function well, for reasons

described in Section 3.1. A new technique to construct sodium coin cells is described in Section 3.4.

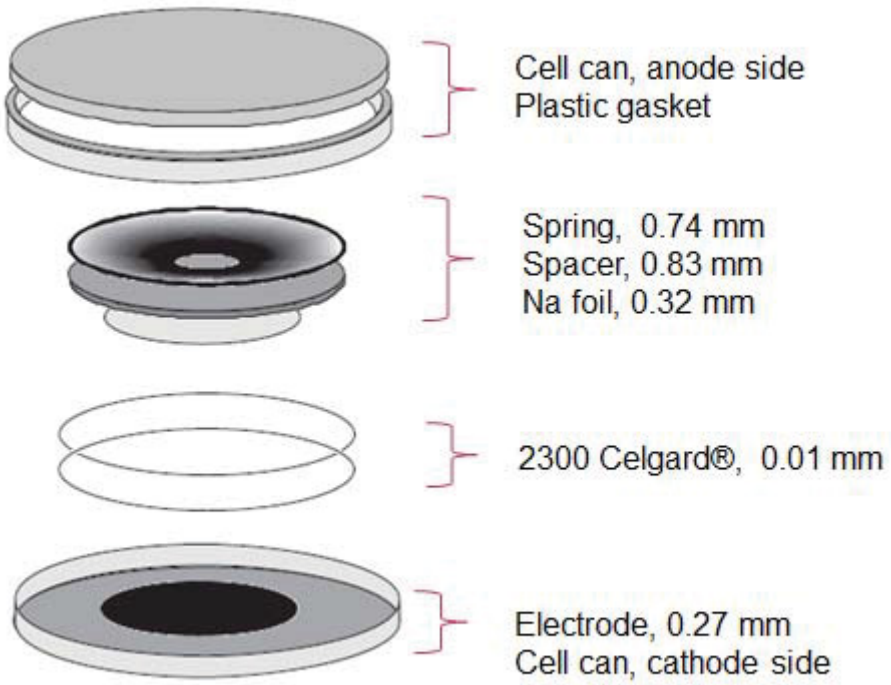

Figure 2.2.2: Lithium coin cell assembly

2.3 X-ray Diffraction Sample Preparation

Two x-ray diffractometers were used in this work. A Siemens D500 diffractometer was used for measurements of air-sensitive samples, and a JD2000 diffractometer was used for in-situ measurements and measurements of air-stable powders. Both diffractometers employ CuKα radiation, a diffracted graphite monochromator and Bragg-Brenato θ:2θ geometry. In both cases a filament current of 30 mA and an accelerating voltage of 40 kV were used to generate x-rays. Unless otherwise stated, measurements were taken in 0.05° steps with a count time of 10 seconds between steps, in the range of 10 to 70° 2θ.

For x-ray measurements, non-air sensitive powder samples were packed into a sample well cut ~5 mm deep into a stainless steel plate and pressed flat with a glass slide to ensure a uniform surface. Air sensitive powder samples were packed in the same way into a specially designed sample stage, shown in Figure 2.3.1, equipped with an aluminized Mylar™ window, and which could be sealed under an inert atmosphere to prevent contact with air. Because of the arched shape of the aluminized Mylar™ window, the window material never satisfied the Bragg condition and therefore did not contribute to the XRD pattern, other than reducing the overall intensity. Gas lines attached to this sample stage allowed it to be purged with helium gas, which is a weak absorber of x-rays due to its low electron density.

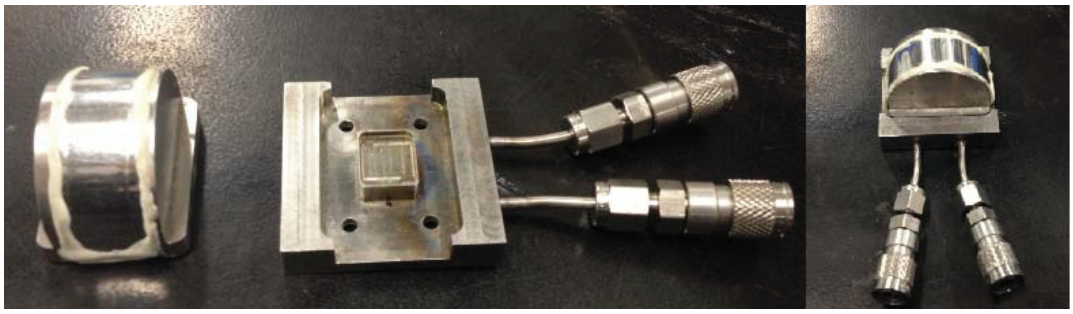

Figure 2.3.1: Powder XRD sample holder for air-sensitive samples.

In-situ x-ray measurements were conducted on electrode powders as they cycled in electrochemical cells. Construction of in-situ coin cells is similar to the construction of half-cells, which is described in Section 3.4 of this thesis, excepting that a beryllium window was glued into a hole cut into the cathode side of the coin cell, so that x-rays could penetrate to the electrode as it was being tested electrochemically. Roscobond®, a water-based contact adhesive was used to fix the beryllium to the inside of the coin cell can prior to assembly. After the coin cell was crimped shut, Torr Seal® was applied to the outside of the coin cell at the beryllium / coin cell can junction to ensure that the coin cell was properly sealed.

2.4 Electrode Fabrication

Thin film electrodes made by sputter deposition and composite electrodes made from powdered materials were both utilized in this study. Sputtered film electrodes were used for electrochemical measurements of silicon, tin, bismuth and lead, (Chapter 4), while composite electrodes were made for measurements performed on hard carbon and active/inactive nanocomposite materials (Chapters 3 and 5). Although aluminium foil can be used as a current collector for sodium-ion anodes, as was mentioned in the introduction, copper foil was used for all electrodes in this work, so that parallel experiments in a lithium coin cell could be made to compare performance if needed.

Sputtering is not a commercially viable way to make electrodes, as it is expensive and energy intensive. Since it is difficult to prepare composite electrode coatings of soft, heavy metals (due to large particle sizes and powder settling in coating dispersions), sputtered films were used for silicon, tin, bismuth, and lead. Additionally, sputtered electrodes do not contain polymer binders or carbon-based conducting diluents, which can react with sodium and obscure the electrochemical behaviour of the active material.

Composite electrode preparation consisted of mixing the active powder with a binder, a conductive diluent (SP carbon black, MMM Belgium) and a binder soluble solvent in a Retsch® PM200 planetary mill at 120 rpm with two ½" tungsten carbide balls until it formed a homogeneous slurry. The slurry was then spread onto copper foil using a doctor blade to form a coating of even thickness. The coating was then air or vacuum dried in an oven until the solvent evaporated, after which was incorporated into a cell (as described in Section 3.4). Since each material required different binder compositions, film thicknesses and heat treatments, further details of each electrode's preparation is discussed within the following sections.

CHAPTER 3 SODIUM-ION COIN CELL OPTIMISATION

3.1 INTRODUCTION

As discussed in Section 2.2, half-cells are the preferred electrochemical test vehicle for the evaluation of new lithium battery materials. Lithium half-cells have poor cycle life, since the lithium metal is continuously reacting with the electrolyte. The decomposition products from this reaction form a thick solid electrolyte interface (SEI) layer on the lithium surface. This impedes the flow of lithium ions to the lithium electrode, increasing impedance and, as a result, cell polarization, causing capacity fade. In addition, lithium does not strip and plate evenly during cycling, causing metal dendrites to form, which grow longer with each cycle. Dendrites can eventually extend through the porous separator, causing an internal short (shunt) when they make contact with the cathode, which may lead to cell failure. In a lithium half-cell, one or two layers of polypropylene separator are sufficient to prevent shunting.

Dendrite formation is much more severe with sodium half-cells [14]. Previous sodium half-cells by Stevens et al. used a polypropylene open mesh (polymesh) layer in addition to two layers of Celgard® polypropylene separator [14]. The purpose of the mesh was to increase the distance between the cell electrodes, so that dendrites would have a longer distance to grow before they caused shunts, thus prolonging cycle life. The gap between mesh fibres is large however, (~2 mm), which leads to an uneven pressure on the anode surface. It is suspected that this causes increased dendrite growth in places with poor stack pressure. Only three half-cycles were shown in the work by Stevens et al., likely because of issues with sodium dendrite growth.

The Komaba group has also published work on sodium in beaker-type half-cells [32]. In beaker cells the electrodes are separated by a large distance and dendrite formation is not a problem. This type of cell is not optimal for testing the commercial relevance of electrode materials since electrodes do not experience the same environment, in terms of pressure and electrolyte availability, as they would in a commercial cell.

To enable sodium-ion resarch, a reliable coin cell construction with the ability to cycle sodium-ion battery materials at least 30 times was needed, so that a material's short term cycle life may be evaluated. Blown microfiber (BMF), a cloth made of fine synthetic fibres has been used internally at 3M™ Company as a compliant separator in coin cells. Although BMF used in this work is thinner than the polymesh separator used by Stevens et al., it was expected to improve cycling over Celgard® separator alone by simultaneously increasing the distance between electrodes, while providing a more even stack pressure. A systematic study of different cell configurations using BMF and Celgard® separator was undertaken to optimise sodium half-cell design and enable future work with sodium in half-cells. Hard carbon was chosen as the working electrode, as its electrochemical characteristics are well known and it has been shown to cycle 200 times in beaker type cells [32].

3.2 Experimental

Hard carbon was prepared from a glucose precursor in the same manner described by Stevens et al [14]. The glucose (>99.5%, Aldrich®) was first dehydrated at 180°C overnight in air, which resulted in a foamy solid. This was ground by hand into a powder,

placed in a quartz boat and loaded into a large tube furnace (Lindberg Blue M). Under a high flow of argon gas, the temperature of the furnace was held at 100°C for an hour (to remove any residual water), then ramped at 1°C per minute to 700°C, held at 700°C for an hour, then cooled to room temperature. The carbon was removed from the tube furnace, ground in an agate autogrinder (AGA, Ishikawa Ltd.), and passed through a 75 μm sieve. Final pyrolysis of the carbon was done in a small tube furnace under vacuum at 1100°C for an hour. The hard carbon was then transferred without exposure to air into an argon glovebox for electrode fabrication.

Electrodes were made in an argon atmosphere by combining hard carbon, polyvinylidene fluoride (PVDF) binder (HSV 900, Kynar®), and carbon black (Super P, MMM Carbon, Belgium) in an 80:12:8 weight ratio. N-methyl-2-pyrrolidone (NMP)(>99.5%, Sigma-Aldrich®) was added to give the slurry a proper viscosity. The mixture was placed in a milling vial with two ½ inch diameter tungsten carbide balls and was dispersed in a planetary mixer for one hour at 120 rpm. The resulting slurry was spread 0.006 inches thick onto copper foil and dried in under vacuum at 120°C for four hours.

Since sodium foil is not commercially available, a method to produce sodium electrodes with consistent thicknesses was developed. The surface of sodium metal chunks (Sigma-Aldrich®, ACS grade), were first scraped clean in an argon filled glovebox to remove their oxide coating. Chunks approximately 2 mm^3 were then placed in plastic bags and passed through a PEPETools® foil roller multiple times, as the nip

distance was decreased. This was repeated until the nip distance, as measured by a feeler gauge, corresponded to a foil thickness between 0.40 and 0.25 mm.

Coin cells were assembled as described in Section 2.2, excepting a sodium foil was used in place of lithium foil. The electrolyte consisted of 1M $NaPF_6$ (98% Aldrich®) in a 1:2 v/v ratio of ethylene carbonate (EC) and diethylcarbonate (DEC), (Novolyte Tech.). A number of separator combinations where tested, shown in Table 3.1 and Figure 3.1. The separator combinations where chosen such that the total stack height approached 2 mm, which is nominal for the coin cell hardware used. Cells made with BMF required more electrolyte in order to fully wet the separator. Coin cells were cycled using a Macoor® Series 4000 Automated Test System at 30°C at a C/10 rate between 5 mV and 2.0 V with a trickle current at the lower cut-off potential of C/20.

Table 3.1: Separator combinations that were tested and the corresponding stack height.

Separator Combination	**Stack Height / mm**
2 layers of 2300 Celgard® (*typical Li coin cell)	2.18
2 layers of 2300 Celgard® + 1 polymesh	2.56
2 layers of 2300 Celgard® + 1 BMF	2.37
2 layers of 2300 Celgard® + 2 BMF	2.56

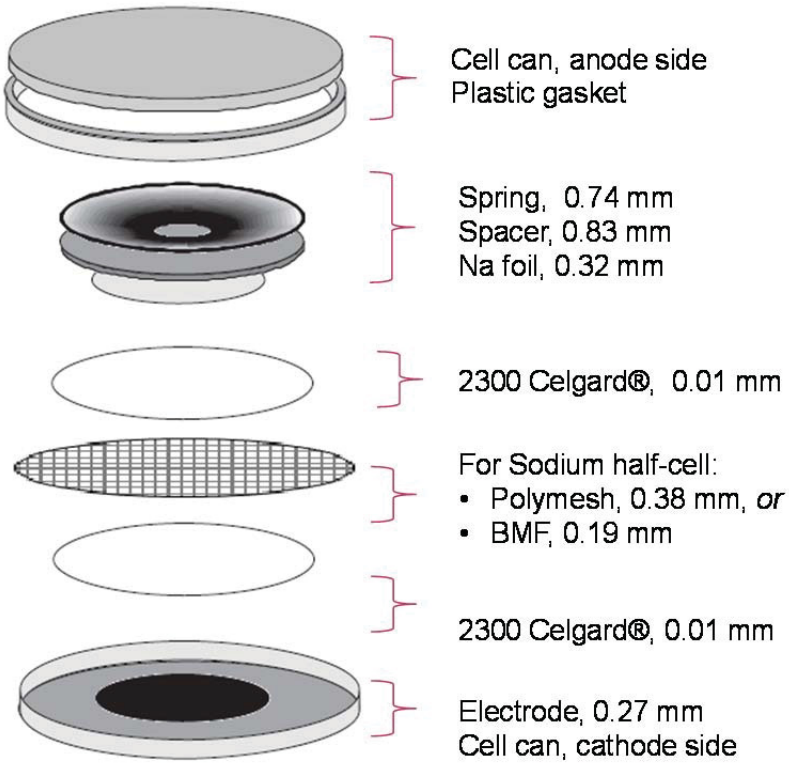

Figure 3.1: Sodium coin cell assembly, as used in this thesis.

3.3 Results and Discussion

Figure 3.2 shows the performance of a sodium-hard carbon half-cell constructed with only two layers of Celgard®, which is the typical lithium half-cell construction. The voltage curve is smooth during each discharge half-cycle, where sodium is being stripped from the metal anode. The voltage curve becomes noisy during each charge half-cycle, where the sodium is being plated back onto the metal surface. This behaviour is typical of shunting caused by dendrites. This also shows that dendrite formation is more severe in sodium coin cells than in lithium coin cells.

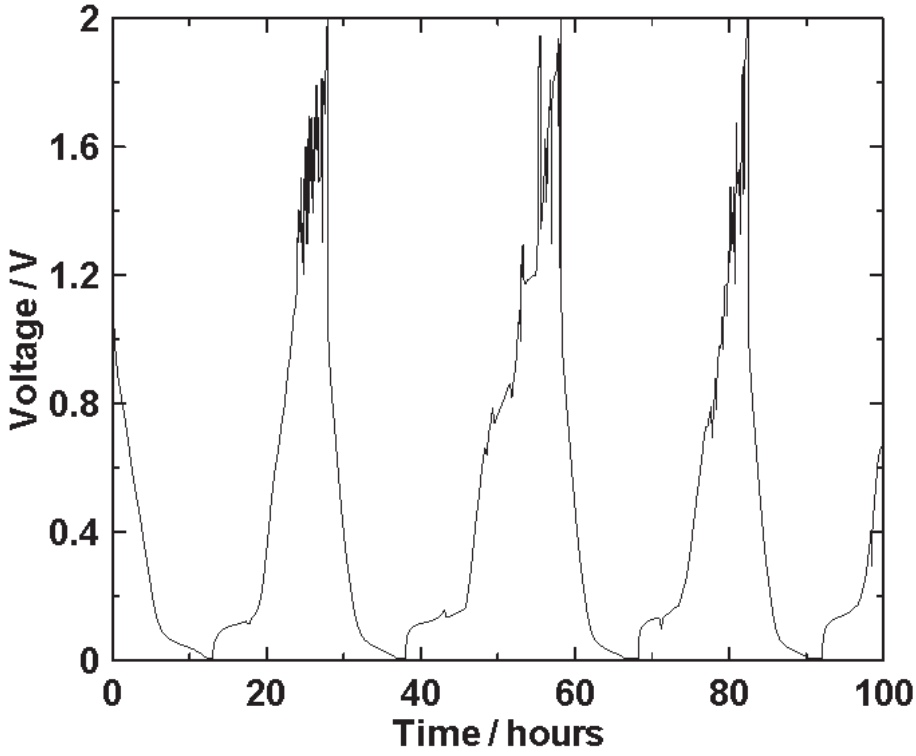

Figure 3.2: Voltage curve of a hard carbon half-cell constructed with two layers of Celgard®.

Figure 3.2 shows the discharge capacity versus cycle number of sodium-hard carbon half-cells with the separator combinations detailed in Table 3.1. Half-cells with only Celgard® as a separator were the first to fail, followed by the half-cells made with polymesh, which had reasonable performance up to 25-30 cycles. Half-cells with one BMF separator performed up to 35-40 cycles, and half-cells with two layers of BMF lasted 40+ cycles.

Although cells made with two layers of BMF outlasted those with one layer of BMF, the stack height for cells with two layers of BMF exceeded the internal height of the void space in the coin cell hardware (Table 3.1). This made crimping the cells

difficult and sometimes resulted in cells bursting open while cycling. Thus it was concluded that two layers of Celgard® and a single layer of BMF separator was the best compromise to observe reversible cycling in a sodium coin cell.

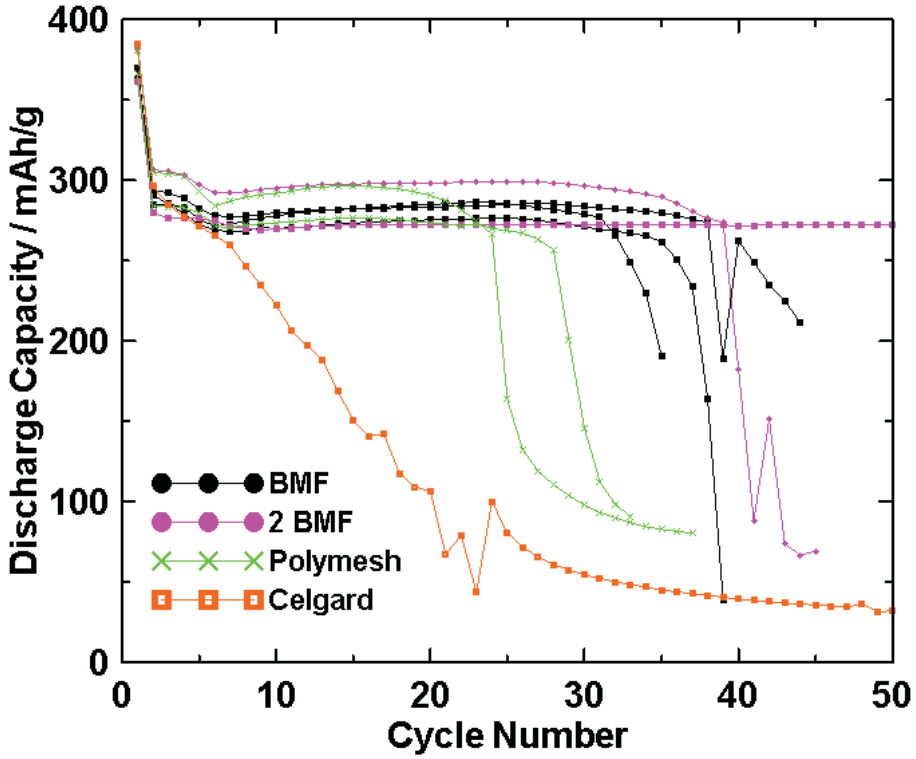

Figure 3.3: Performance of sodium-hard carbon half-cells with the separator combinations shown in Table 3.1.

3.4 Conclusion

It was found that with only 2300 Celgard® separators, sodium coin cells did not perform well and failed after less than one cycle, due to severe dendrite formation. Additional separators, polymesh and BMF, were added to the separator stack in order to increase the distance between electrodes, which would require dendrites to grow longer before inducing an internal short. It was found that the use of one BMF separator

produced longer cycle life (>35 cycles) than one polymesh separator (>25 cycles). It is thought that this is because BMF creates a more even pressure on the sodium electrode.

This work allowed sodium half-cells to be standardised for use in the rest of this thesis. All the coin cell data presented in this thesis were obtained from coin cells made using the standardised method described above: with a spring, spacer, hand-rolled sodium foil anode, 1M $NaPF_6$ in 1:2 v/v EC:DEC electrolyte, one layer of BMF sandwiched between two layers of Celgard™ 2301 separator, and a working electrode, all sealed under argon,. With this set up, the coin cells could be expected to perform without cell component failure for at least 30 cycles.

CHAPTER 4 ELECTROCHEMICAL ALLOYING OF SODIUM WITH THE ELEMENTS

4.0 Sodium alloys

4.0.1 Introduction

As discussed in Chapter 1, alloy anodes have gained much attention in the lithium-ion battery field as they offer far superior volumetric and gravimetric capacities than conventional graphite-based anodes. In order to determine if alloy anodes could be utilized in sodium ion batteries and to design advanced active/inactive alloys, the alloying behaviour of the elements with sodium needs to be investigated. According to reference [25], Ag, Au, Ba, Bi, Cd, Ga ,Ge, Hg, In, Pb, Pd, Pt, Sb, Se, Sn, Te, Th and Tl form binary alloys with sodium. Intermetalic phases of silicon and sodium are also known [33]. Of all these elements silicon, tin, lead, bismuth and antimony are the most interesting candidates on which to base sodium alloy anodes, since the other elements are acutely toxic or prohibitively expensive.

Sodium insertion in antimony has been described recently by others [34, 35]. Antimony based alloys have been shown to have long cycle life with high capacity. Sodiation of antimony was found not to follow the binary equilibrium phase diagram. The following sections will discuss the electrochemistry and the structural changes induced by sodium insertion in silicon, tin, lead and bismuth in order to evaluate their performance as sodium-ion anodes.

4.0.2 EXPERIMENTAL

Sputtered electrodes were prepared using a modified Corona Vacuum Coaters Inc. V-3T deposition system equipped with a 500 L/s turbo pump and a Polycold® system. The sputtering targets were 5.08 cm in diameter and covered by a mask such that the thickness of the sputtered films would vary linearly along the radius of the sputtering track deposited on a rotating copper foil substrate. This allowed selection of electrodes of different thicknesses and capacities. A base pressure of 8×10^{-7} Torr with 1.5 mT argon pressure and 50 W of power were used for deposition. Details of the sputtering systems at Dalhousie University have been described elsewhere [36].

Lead composite electrode coatings, which are discussed in Section 4.3.3, were made by combining lead powder (99%, -325 mesh, Sigma Aldrich®), SP carbon black (MMM, Belgium) and polyamic acid (19.2 % in NMP, HD Microsystems™ PI-2555) in a 9:6:4 weight ratio with added NMP (<99.5%, Aldrich®) for consistency. The slurry was mixed in a Retch PM200 planetary mill at 120 rpm, coated with a 0.006" gap doctor blade onto copper foil, dried under vacuum at 150°C for two hours, and further heated to 300°C under vacuum for two hours in order to convert the polyamic acid to polyimide, the desired binder, through a condensation reaction.

Electrodes were incorporated into coin cells, as described in Section 3.3, after which they were subjected to electrochemical tests using a Maccor® Series 4000 Automated Test System. For tin and lead half-cells, a high current was applied until the voltages of the cells were below 0.8 V to avoid anomalous high voltage irreversible capacity (AHVIC), which will be discussed in detail in Sections 4.2 and 4.3. The coin

cells were then cycled at 30°C, between 5 mV and 1 V at a rate of C/50 (C being the calculated theoretical capacity based on the most sodiated phase from the binary alloy phase diagram). After a voltage of 5 mV was reached, the cells were held at constant potential until the current decreased to C/100, before the next desodiation half-cycle.

In-situ cell electrodes were made according to the description in 2.3. After assembly, in-situ cells were placed in a JD2000 diffractometer equipped with a copper x-ray source and a diffracted beam monochromator and connected to a Moli Energy® charging system. XRD patterns for in-situ studies of tin and lead electrodes were measured from 15 to 60°, with 0.05° per step and a count time given in Table 4.0.1. All measurements were conducted at room temperature. Parameters for the electrochemical tests are given in Table 4.0.1.

Table 4.0.1: Experimental parameters for in-situ XRD tests

Cell	Initial discharge current / mA	Cycling current / mA	Voltage limits	XRD count time
Tin	3C for 60 seconds	C/50	5mV to 0.8 V	7 sec/ step
Lead	6C for 60 seconds	C/50	5mV to 1.5 V	7 sec/step
Bismuth	none	C/25	5mV to 1.7 V	8 sec/step

4.1 Sodium Insertion into Silicon

4.1.1 Introduction

No equilibrium binary phase diagram has been repoted for the Na-Si system, although four intermetallic Na-Si phases have been reported: NaSi, Na_2Si, Na_4Si_{23} and $NaSi_{94}$ [33]. The fully sodiated NaSi phase corresponds to a capacity of 954 mAh/g or 912 mAh/cm^3, with 144% volume expansion at full sodiation. This is greater than the specific and volumetric capacity of hard carbon, which are 300 mAh/g and 630 mAh/cm^3 [14]. A voltage curve of the sodiation of silicon calculated with density functional theory (DFT), taking into account only the formation of NaSi, was reported to have a single voltage plateau at 0.5 V [37].

4.1.2 Experimental

Sputtered silicon electrodes were made and tested in electrochemical cells vs. sodium metal as described in Section 4.0.2.

4.1.3 Results and Discussion

Figure 4.1.1 shows the voltage curve obtained from a sodium half-cell with a sputtered silicon working electrode. 200 mAh/g of non-reversible capacity is observed during the first discharge of the cell. This corresponds to 1/5th of the theoretical sodiation capacity of silicon. Subsequent cycling of the cell between 5 mV and 0.9 V did not result in any reversible capacity. The irreversible capacity observed during the first discharge could be due to SEI formation. Since the sputtered electrode had only ~0.5 mg of active material, irreversible capacity from SEI formation would appear large when plotted per

unit mass of silicon. However, the pleateau at 0.4 V could correspond to the plateau at 0.5 V predicted by Chevrier [37]. Other small features in the voltage curve during the first discharge could also be due to the formation of other Na-Si compounds. It is possible that this system suffers from poor sodiation kinetics and requires elevated temperature, smaller currents, and smaller particle size for sodiation to be achieved.

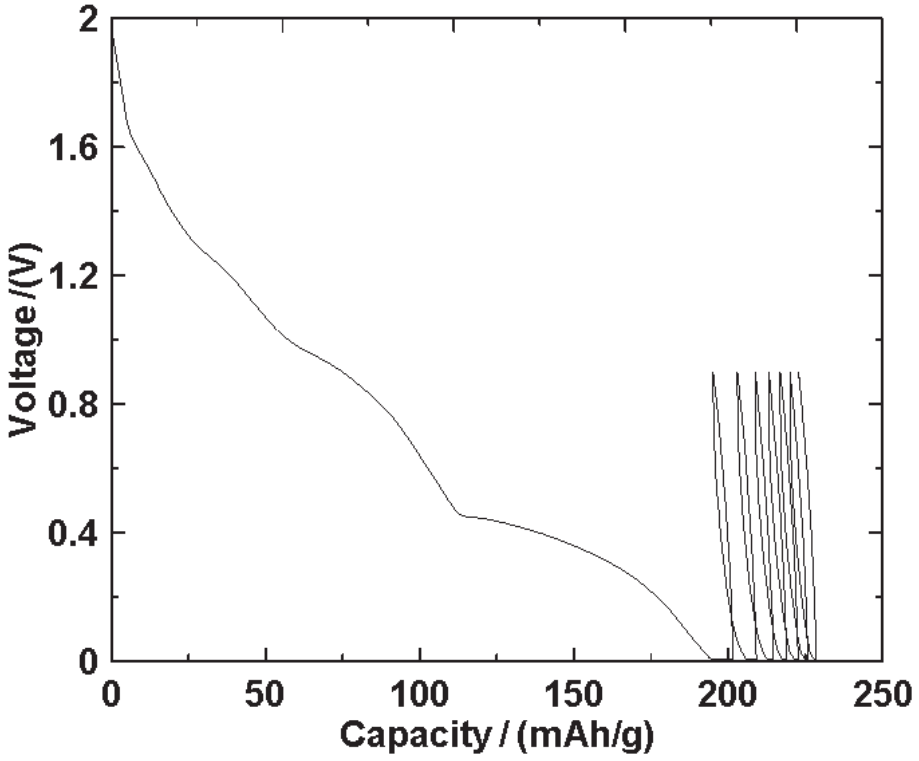

Figure 4.1.1: Voltage vs. specific capacity of a silicon-sodium half-cell.

4.1.4 CONCLUSION

The sodiation of sputtered silicon electrodes at 30°C resulted in a first discharge capacity of 200 mAh/g. It is unclear whether this capacity is due to SEI formation or to sodium insertion in the silicon electrode. A small plateau at 0.4 V, close to the predicted voltage of 0.5 V, indicates that the latter could be the case. It is possible that full

sodiation is not observed due to slow kinetics. Further studies at higher temperatures, lower currents and smaller particle sizes are needed to fully understand sodium insertion behaviour in this system.

4.2 Sodium Insertion into Tin

4.2.1 Introduction

Tin based anodes for lithium-ion batteries have been studied extensively [38-40]. Out of the six known equilibrium binary Li-Sn phases, only Li_2Sn_5 and LiSn were observed during the lithiation of tin [39]. Instead, related phases with only short range ordering were formed. It was suggested that the equilibrium Li-Sn phases with long range ordered structures do not form during room temperature lithiation because of poor kinetics [39].

During the lithiation of electroplated or sputtered tin films, Beattie and co-workers described the occurrence of AHVIC at 1.4 V vs. Li [41]. AHVIC was attributed to the catalytic decomposition of electrolyte on clean tin surfaces. AHVIC could be avoided if a sufficiently high current pulse was initially applied to the cell, such that the tin voltage was forced below the Li-Sn alloying potential. During this pulse Li-Sn alloy phases, which do not catalyze electrolyte decomposition, are thought to be formed on the tin surface. After this initial high current pulse, lithiation at low currents may be performed with little electrolyte decomposition [41].

Very little research on alloy negative electrodes for sodium-ion batteries has been reported so far. An early report from 1920 studied the open circuit potentials of Na-Sn alloys prepared from melting of the elements in hydrogen gas. Five plateaus in the potential were observed, corresponding to the existence of five intermetallic Na-Sn alloy

phases [42]. In 1928 the binary phase diagram of sodium and tin was published [43], with $NaSn_6$, $NaSn_4$, $NaSn_3$, $NaSn_2$, Na_9Sn_4, Na_3Sn and $Na_{15}Sn_4$ listed as the thermodynamically stable Na-Sn phases at ambient temperatures. In 1990 Huggins, measured the open-circuit potentials with respect to sodium at 120°C of Na-Sn alloys prepared by melting of the elements or by coulometric titration [44]. In this study only three Na-Sn alloy phases were observed, as opposed to the seven shown in the equilibrium phase diagram. It was suggested that the equilibrium phase diagram may be insufficient to describe the Na-Sn system at low temperatures. In 2011, Chevrier et al. published a voltage curve for sodium insertion into tin based on DFT calculations of only the Na-Sn phases with crystal structures listed in the Inorganic Crystal Structure Database (ICSD): $NaSn_5$, NaSn, Na_9Sn_4, $Na_{15}Sn_4$ [37]. The calculated voltage curve was almost identical to the experimental results of Huggins, excepting Chevrier included the $NaSn_5$ phase in his calculations, which is a phase beyond the range of compositions examined by Huggins. As a result, Chevrier's calculated voltage curve has an additional fourth plateau. Very recently Komaba et al demonstrated sodium insertion into Sn-polyacrylate electrodes, and showed by XRD that the phase of maximum sodiation corresponds to $Na_{15}Sn_4$ [45]. A tin electrode sodiated to this composition had a reversible capacity of 847 mAh/g and 1177 mAh/cm^3.

The purpose of this work was to investigate the structural changes that occur during the electrochemical insertion of sodium into tin at ambient temperatures. In-situ XRD measurements of the tin electrode during cycling allowed a detailed look at how the structure of tin changes upon sodium insertion. At ambient temperatures it was found that the Sn vs. Na voltage curve consisted of four distinct plateaus, indicating that four

Na-Sn phases are formed. At full sodiation, the $Na_{15}Sn_4$ phase was observed, which is the thermodynamically stable binary phase at this composition. The crystal structures of the three other intermediate Na-Sn phases do not correspond to any of the reported Na-Sn phases. One of these phases, with composition close to that of NaSn was found to be amorphous.

4.2.2 Experimental

Sputtered tin electrodes were incorporated in coin cells and tested as described in Section 4.0.2. An in-situ XRD cell was made and tested as described in Section 2.3 and Table 4.0.1.

4.2.3 Results

Discharging (sodiation of Sn) sputtered Sn vs. Na cells at a slow rate resulted in a long voltage plateau at 1.4 V. We attribute this behaviour to the same catalytic electrolyte decomposition reactions that produce AHVIC in Li vs. Sn cells [41]. By first applying a high current pulse, as described above, AHVIC could be completely avoided. Figure 4.2.1 shows the voltage curve for the first three half-cycles of a Sn vs. Na coin cell after a short 1 mA current pulse was applied to avoid AHVIC. A first discharge capacity of 864 mAh/g was achieved, which is close to the theoretical capacity of 847 mAh/g, assuming the formation of $Na_{15}Sn_4$ as the fully sodiated phase.

The voltage curve in Figure 4.2.1 has four distinct plateaus of constant voltage during both the sodiation and desodiation half-cycles, corresponding to four Na-Sn two-phase regions. The plateaus will be referred to as 1, 2, 3, and 4, in order of increasing

sodiation, as shown in Figure 4.2.1. Curiously the voltage is seen to increase with sodiation on plateau 1. Since this is thermodynamically impossible, it must be associated with the sodiation kinetics. One explanation for this behaviour is that diffusion in the electrode is improved as sodiation progresses. This would tend to reduce polarization during sodiation, causing an increase in voltage. The same behaviour occurs during the desodiation half-cycle. Here the plateau 1 voltage decreases during desodiation, possibly since diffusion is improving as the alloy is desodiated.

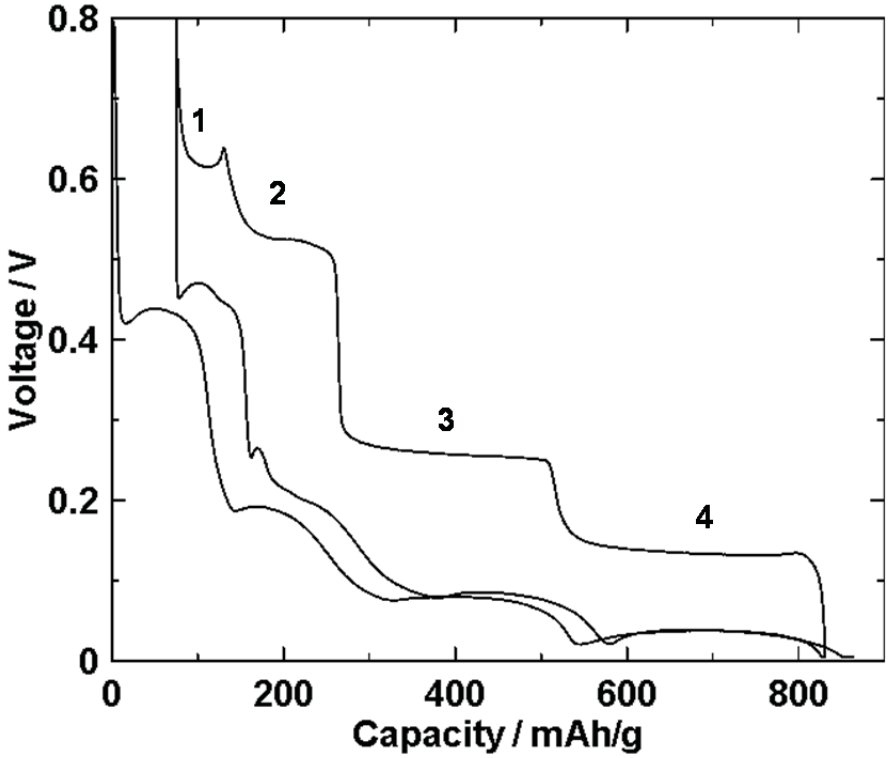

Figure 4.2.1: Voltage vs. specific capacity plot showing the reversible insertion of sodium in sputtered tin.

In Figure 4.2.2, the cell voltage is potted versus atomic percent tin and is superimposed on the sodium-tin binary alloy phase diagram [43]. Many of the two-phase regions indicated in the equilibrium phase diagram are absent in the voltage curve. However, the last three plateaus of the voltage curve are coincidental with the formation of NaSn, Na_9Sn_4, and $Na_{15}Sn_4$.

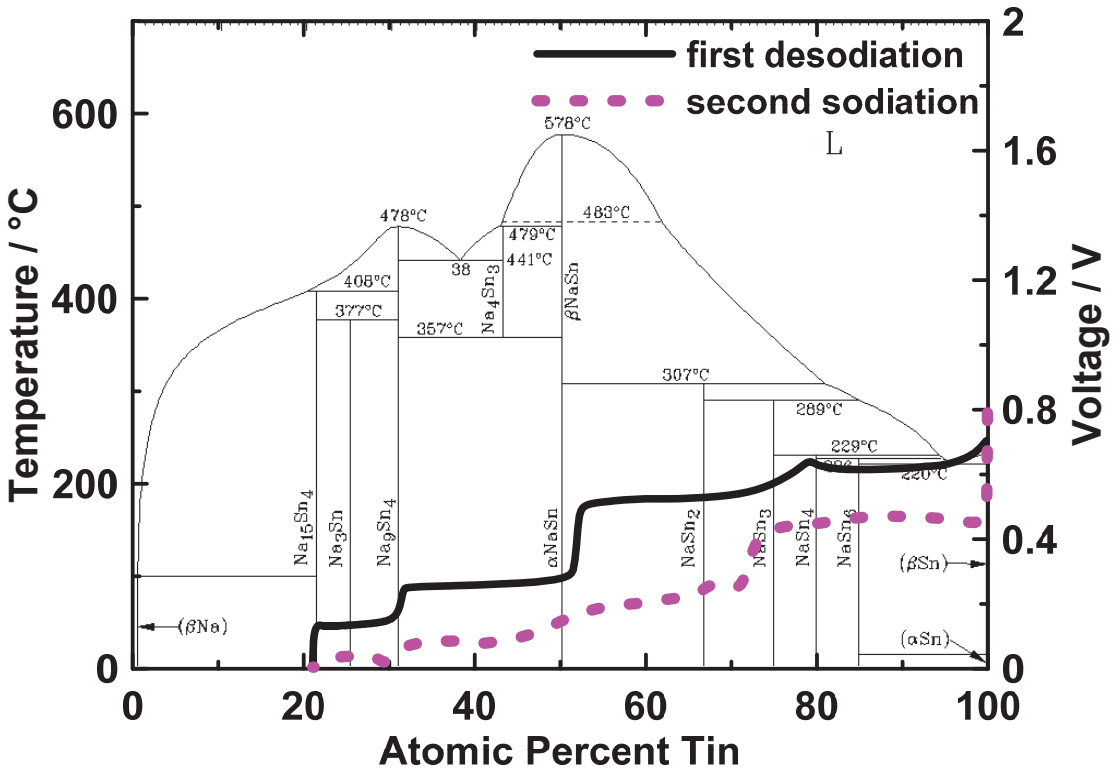

Figure 4.2.2: Voltage curves of the first desodiation and second sodiation half-cycles of sputtered tin from Figure 4.2.1 superimposed on the Na-Sn binary phase diagram [43].

Figure 4.2.3 shows the voltage curve from Figure 4.2.1 superimposed on the voltage curve Chevrier calculated by DFT [37] and data points digitized from Huggins' open circuit voltage measurements of Na-Sn phases at 120° C [44]. DFT calculations were done using only the crystal structures of Na_xSn found in the ICSD that had complete

atomic positions. As such, some of the phases shown in the phase diagram of Figure 4.2.2 were not taken into consideration in Chevrier's calculation [37]. Nevertheless, all three voltage curves are in general agreement, shown by Figure 4.2.3, with respect to the length and voltages of the plateaus, excepting for plateau 1. Here the DFT calculated voltage is much higher and the capacity is shorter than what is observed experimentally. This is likely because the $NaSn_5$ phase used in the DFT calculations is not what is observed to form by XRD measurements, as will be shown below. No open circuit potential measurements were reported by Huggins in this composition region [44].

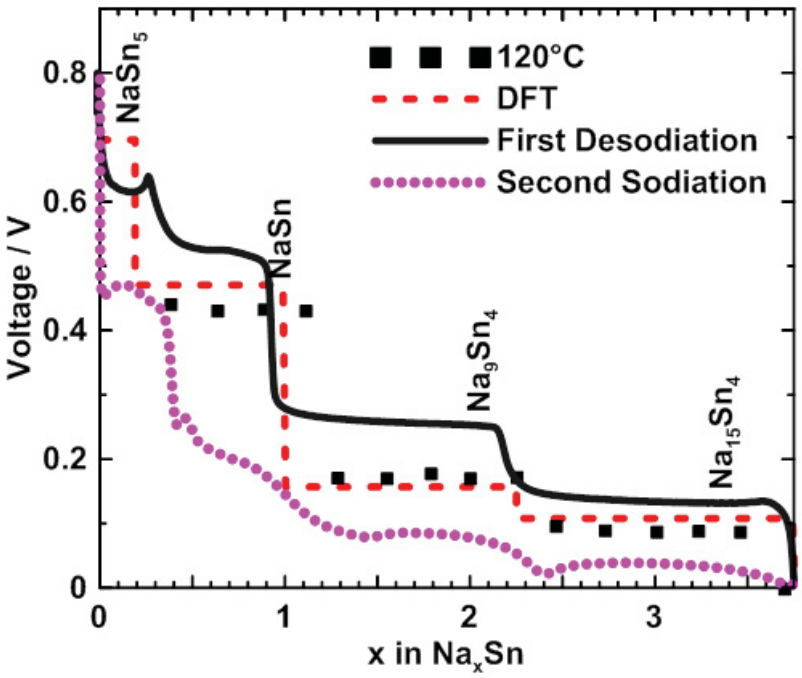

Figure 4.2.3: Voltage curves of the first desodiation and second sodiation of sputtered tin, superimposed on the predicted DFT voltage curve [37], and open circuit measurements taken at 120° by Huggins [44].

In-situ XRD patterns for the sodiation of tin are shown in Figure 4.2.4 alongside the corresponding voltage curve. The voltage curve is similar to what was obtained in a regular coin cell, excepting that during plateau 3 of the first desodiation half-cycle the voltage suddenly increases and becomes noisy. It is not known why this occurred, but

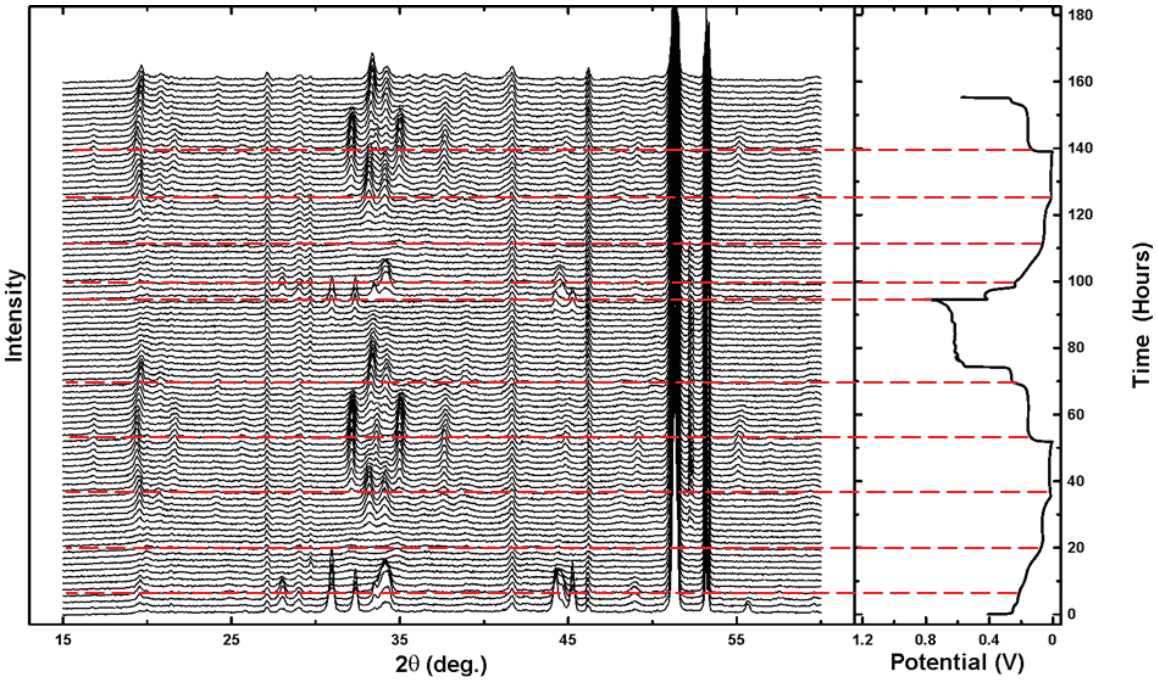

Figure 4.2.4: in-situ XRD data and the corresponding voltage curve. Dashed lines separating the two-phase regions as indicated by the voltage curve are added as a guide to the eye.

may be due to electrical connection issues either internally or external to the cell. The cell recovered from this behaviour during the next sodiation half-cycle. Changes in the XRD patterns during cycling confirm the two-phase behaviour indicated by the voltage curve. During sodiation on plateau 1, crystalline tin peaks decrease in intensity, and then vanish as peaks from a new crystalline phase are formed. These peaks then disappear during sodiation on plateau 2 and a fully amorphous phase is formed. Upon further

sodiation a new crystalline peak is formed during plateau 3. Finally, these peaks disappear and are replaced with another crystalline phase during sodiation on plateau 4.

During desodiation, the voltage curve of the non in-situ cell shown in Figure 4.2.1 would indicate that the desodiation process is exactly the reverse of the sodiation process. In the in-situ cell desodiation is indeed seen to occur as the reverse of the sodiation process during plateau 4 and plateau 3. However, the phase formed during plateau 2 during sodiation is not observed by in-situ XRD during the desodiation half-cycle. Instead this phase is skipped and tin is directly formed from the amorphous phase. It is most likely that this behaviour is caused by the previously mentioned cell malfunction, which forced the in-situ cell to high voltage during desodiation plateaus 3, 2 and 1. The voltage curve in Figure 4.2.3, however, clearly shows that that the plateaus occurring during discharge are exactly reproduced during charge, which is evidence that the sodiation and desodiation mechanisms are identical. The second sodiation half-cycle is then seen to follow the same behaviour as the first sodiation half-cycle. During the second desodiation half-cycle the in-situ cell stopped operating.

Figure 4.2.5 shows the XRD pattern measured at the end of plateau 1 during the first sodiation half-cycle of the in-situ cell. The composition of this phase, as determined by coulometry, corresponds roughly to $NaSn_3$. However, the diffraction pattern observed does not correspond with any known Na-Sn phase. Evidently a new Na-Sn phase is formed with an approximate composition of $NaSn_3$. Figure 4.2.6 shows the XRD pattern measured at the end of plateau 2 during the first sodiation half-cycle of the in-situ cell,

corresponding roughly to the composition NaSn. The majority of the area comprising this pattern comes from an amorphous phase, excepting some minor peaks at 20, 32, and 35 degrees, which could not be identified. Figure 4.2.7 shows the XRD pattern measured at the end of plateau 3 during the first sodiation half-cycle of the in-situ cell, corresponding roughly to the composition Na_9Sn_4. The XRD pattern consists of crystalline peaks that do not correspond to any reported Na-Sn phase. Finally, Figure 4.2.8 shows the XRD pattern measured at the end of plateau 4 during the first sodiation half-cycle of the in-situ cell, corresponding roughly to the composition $Na_{15}Sn_4$. A Rietveld refinement was used to fit this pattern to the parameters for $Na_{15}Sn_4$ from [46]. Cell part peaks were excluded from the refinement. The results of this refinement are shown in Table 4.2.1 and Figure 4.2.8. The lattice constant was found to be 13.19 Å, which is close to 13.14 Å, the value reported in [46].

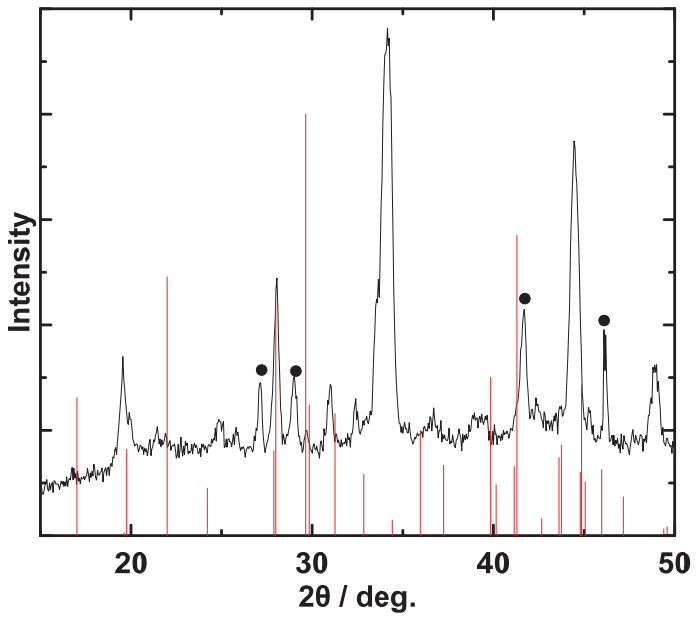

Figure 4.2.5: In-situ XRD pattern of the sodiated tin phase formed at the end of plateau 1. Expected peak positions and intensities for $NaSn_5$ are indicated by vertical lines. Peaks from beryllium and cell parts are labelled with black dots.

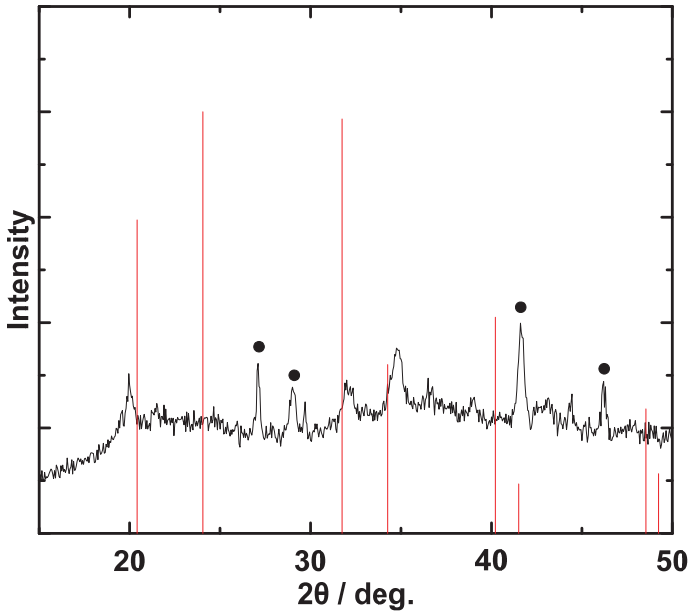

Figure 4.2.6: In-situ XRD pattern of the sodiated phase formed at the end of plateau 2. Expected peak positions and intensities for NaSn are indicated by vertical lines. Peaks from beryllium and cell parts are labelled with black dots.

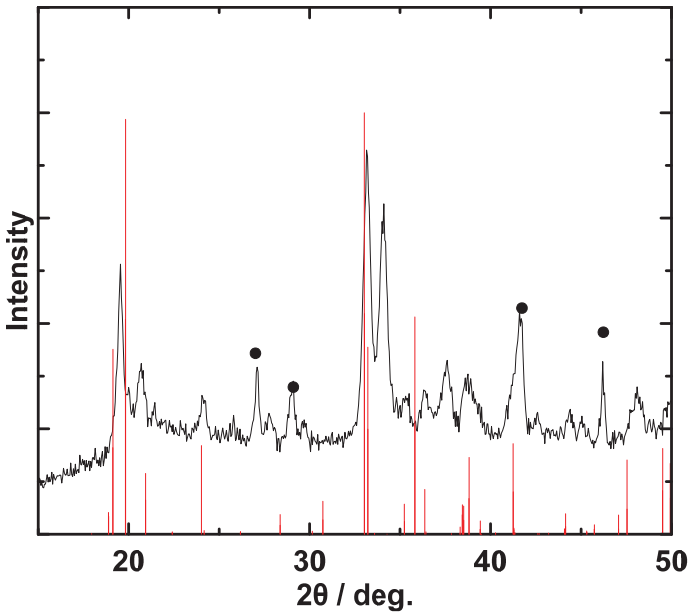

Figure 4.2.7: In-situ XRD pattern of the sodiated phase formed at the end of plateau 3. Expected peak positions and intensities for Na_9Sn_4 are indicated by vertical lines. Peaks from beryllium and cell parts are labelled with black dots.

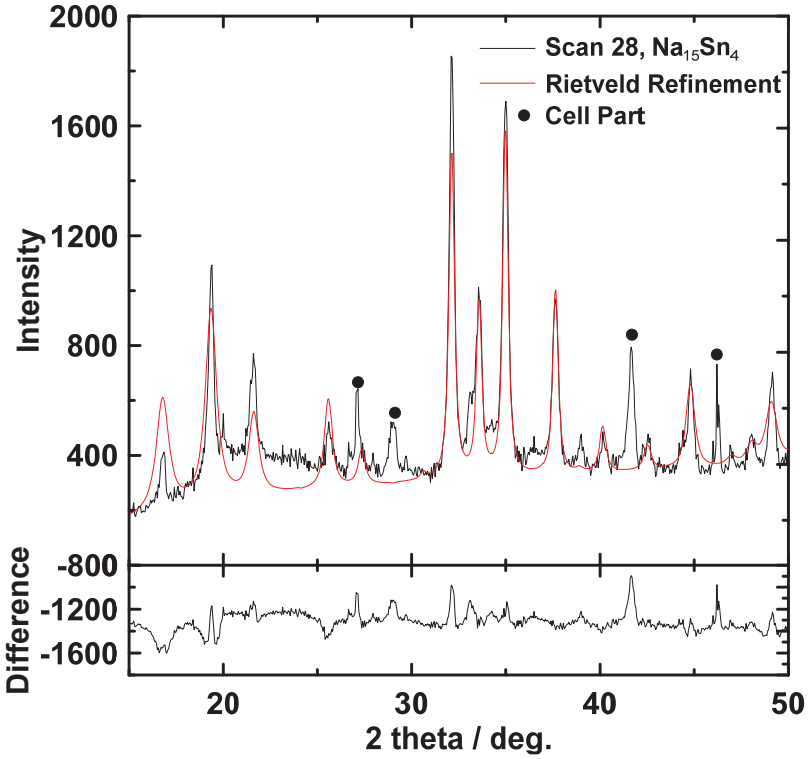

Figure 4.2.8: In-situ XRD pattern of the sodiated phase formed at the end of plateau 4 in black and the fit from the Rietveld refinement in red. Below is the difference between experimental and calculated patterns.

Table 4.2.1: Parameters obtained from the Rietveld refinement of scan 28 to $Na_{15}Sn_4$[46].

Phase			$Na_{15}Sn_4$	
Space Group			I-43d	
Z			4	
a /Å			13.1(9)	
Bragg R.			5.25	
Atom	**Site**	**x**	**y**	**z**
Sn	16c	0.375	0	0.25

Na_1	12b	0.2083	0.2083	0.2083
Na_2	48e	0.12(4)	0.17(2)	0.97(8)

4.2.4 DISCUSSION

Considering the in-situ XRD results, the electrochemical sodiation of Na with Tin follows the following reaction steps:

$$\text{Plateau 1: } Na + Sn \rightarrow NaSn_3^*$$

$$\text{Plateau 2: } Na + NaSn_3^* \rightarrow \text{a-NaSn}$$

$$\text{Plateau 3: } 5Na + 4(\text{a-NaSn}) \rightarrow Na_9Sn_4^*$$

$$\text{Plateau 4: } 6Na + Na_9Sn_4^* \rightarrow Na_{15}Sn_4,$$

where 'a' indicates the formation of an amorphous phase and (*) indicates a new crystalline phase with approximate stoichiometries, as determined by coulometry.

The only phase observed to form during the sodiation of tin having a crystal structure corresponding to a known Na-Sn phase was $Na_{15}Sn_4$. This phase has a simple crystalline structure composed of isolated tin atoms surrounded by sodium atoms [46]. $Li_{15}Si_4$ has the same structure as $Na_{15}Sn_4$ and is also formed during the lithiation of silicon [17]. Other binary phases of Na-Sn listed in the ICSD are more complex: $NaSn_5$ consists of tetragonally coordinated tin forming a complex net square planes and pentagonal dodecahedrons [47], while Na_9Sn_4 is composed of Sn dimers arranged in a lattice with a large superstructure, 30 Å in extent [46]. The inability of tin and sodium atoms to arrange into complex structures at room temperature may be why the expected

thermodynamically stable phases do not form. The same behaviour has been observed during the lithiation of tin [39].

In contrast to the above arguments, the NaSn structure is relatively simple, being composed of tin tetrahedra surrounded by sodium atoms, but crystalline NaSn was not observed to form during tin sodiation. Instead, Figure 4.2.6 shows broad peaks of increased background intensity, indicating that an amorphous phase forms when tin is sodiated to this composition. The small peaks that could not be identified suggest the existence of another new phase. It could be that the conversion to this phase is slow, and hence the structure is only partially formed from the amorphous phase. According to the Na-Sn phase diagram, shown in Figure 4.2.2, NaSn is the highest melting Na-Sn binary phase [25]. This is an indication of low atom mobility and might explain why an amorphous phase is formed at this composition.

4.2.5 Conclusion

During the sodiation of tin AHVIC was observed and could be avoided with an initial high current pulse, as has been described for the lithiation of tin. The full sodiation of tin resulted in a discharge capacity of 847 mAh/g, which corresponds well with the formation of $Na_{15}Sn_4$; the thermodynamically stable Na-Sn phase with the highest sodium content. The Na vs. Sn voltage curve consisted of four distinct plateaus corresponding to the formation of four Na-Sn phases in two-phase regions. In-situ XRD confirmed the formation of crystalline $Na_{15}Sn_4$ at full sodiation. The three intermediate

Na-Sn phases formed during tin sodiation were found to be new phases that are not predicted by the equilibrium phase diagram. Two of these phases were crystalline with XRD patterns that do not correspond to any of the known Na-Sn binary phases, while an amorphous phase is formed near the composition NaSn. It is proposed that, as in the Li-Sn system, complex Na-Sn phases are unlikely to form during room temperature sodiation, resulting in the formation of new simple crystal structures instead of the more complex thermodynamically stable phases. The formation of an amorphous phase at the NaSn composition is likely due low atom mobility at this composition.

4.3 Sodium Insertion into Lead

4.3.1 Introduction

Sodium has previously been shown to electrochemically insert into lead at room temperature [45,9]. Impressive reversibility was demonstrated by Jow et al. when a poly(p-phenylene) based binder was used, resulting in many hundreds of cycles with little capacity fade [9]. The voltage curve of lead was found to closely match the equilibrium Na-Pb phase diagram. From the similarity of the voltage curve to the Na-Pb phase diagram it was suggested that $NaPb_3$, NaPb, Na_5Pb_2, and $Na_{15}Pb_4$ sequentially form as lead is sodiated.

Here, a careful study was undertaken to understand the structural changes that occur during the of sodium insertion into lead. During initial sodiation, AHVIC was observed to occur. Similar to the metallation of tin, AVHIC could be avoided if the lead was initially forced to low potentials prior to cycling. In-situ XRD measurements indicated that the equilibrium phase diagram was generally followed during sodiation of lead. Na_5Pb_2 was the only phase predicted by the equilibrium phase diagram that was not observed by XRD during sodiation. It is suspected that this phase was not formed because of poor kinetics.

4.3.2 Experimental

Both sputter deposited electrodes and composite electrodes were used in this study. The formulation of these electrodes is described in Section 4.0.2. Coin cell

preparation is described in Section 3.4 and in-situ XRD cells were made and tested according to Section 2.33 and Table 4.01.

4.3.3 Results and Discussion

During the initial sodiation of lead, severe AHVIC was observed. AHVIC was successfully avoided if the cell voltage was held below the voltage of the first plateau for 20 seconds. This required a current of ~1.7C. Figure 4.3.1 shows the voltage curve of the first cycle of a lead half-cell. The voltage curve is similar to what Jow et al. observed previously [9]. During each half-cycle, four plateaus of constant voltage are observed, indicating four Na-Pb two-phase regions. A capacity of 317 mAh/g was obtained during the first discharge, which approaches the theoretical capacity of the most sodiated Na-Pb

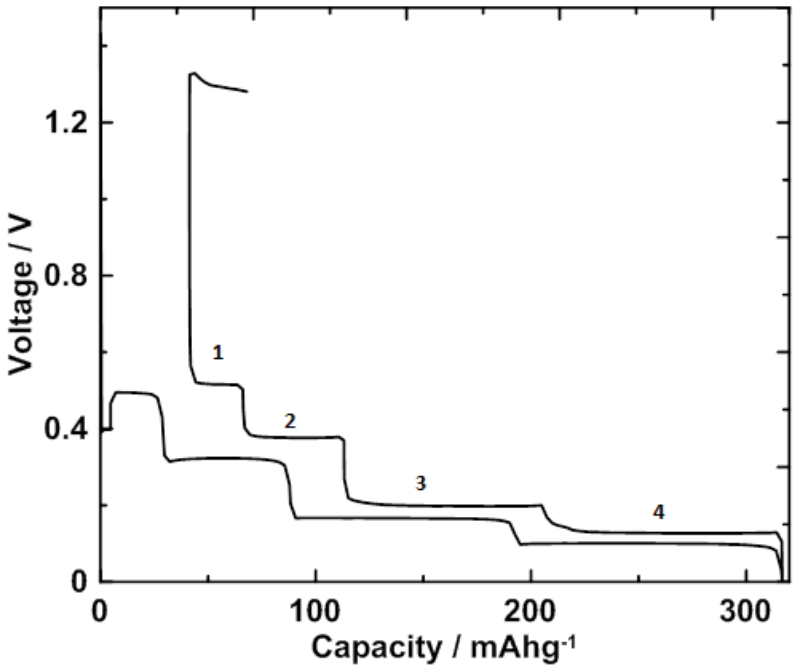

Figure 4.3.1: Voltage curve displaying reversible insertion of sodium into sputtered lead.

phase ($Na_{15}Pb_4$), 485 mAh/g. When the electrode was fully desodiated at the end of the first charge, the cell voltage jumped to 1.3 V, beyond the programmed upper voltage cut-off of 1 V. A discharge current was then applied, but the voltage remained high and regular cycling did not resume. This is likely due to AHVIC.

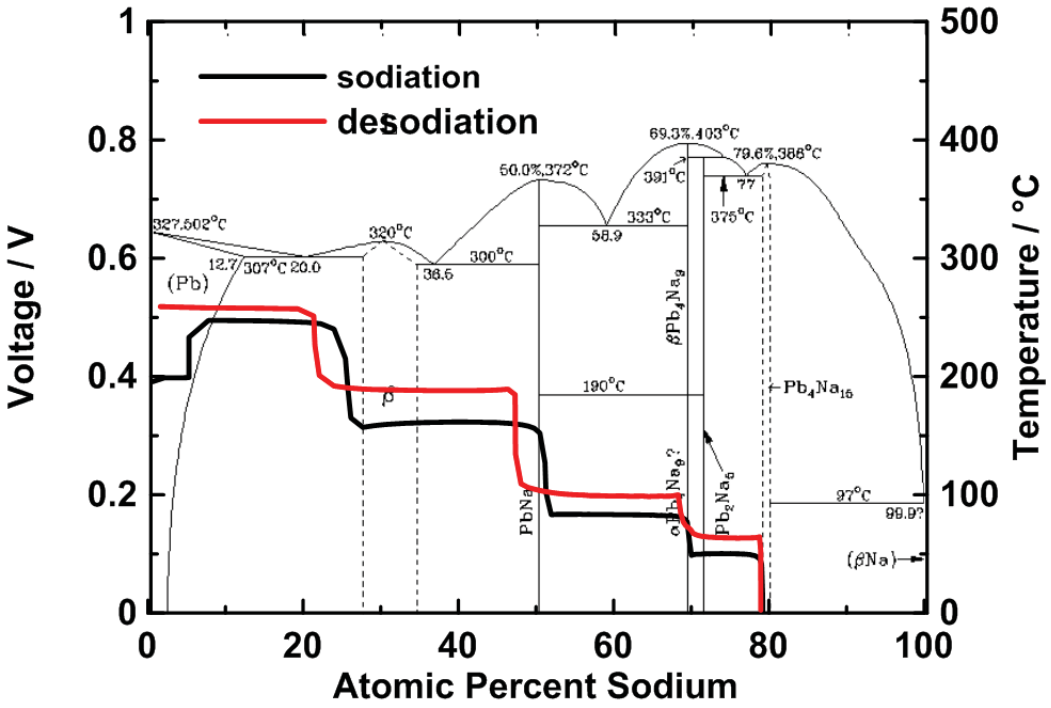

Figure 4.3.2: Voltage curve of the first cycle of sputtered lead from figure 4.3.1 overlaid onto the Na-Pb binary phase diagram [25].

Figure 4.3.2 shows the same voltage curve as Figure 4.3.1, plotted vs. atomic percent sodium overlaid onto the Na-Pb binary alloy phase diagram [25]. All phases shown in the diagram appear to be formed during sodiation, as indicated by the locations of the plateaus in the voltage curve, excepting Na_5Pb_2.

During desodiation, a small plateau near the composition of Na_5Pb_2 suggests that this phase may be forming. The differential capacity of the voltage curve in Figure 4.3.1 is plotted vs. voltage in Figure 4.3.3. While four peaks are present during the initial sodiation, five are present during desodiation. The presence of the small peak at 0.32 V during desodiation could indicate that Na_5Pb_2 is formed during desodiation but not during sodiation where the peak is absent.

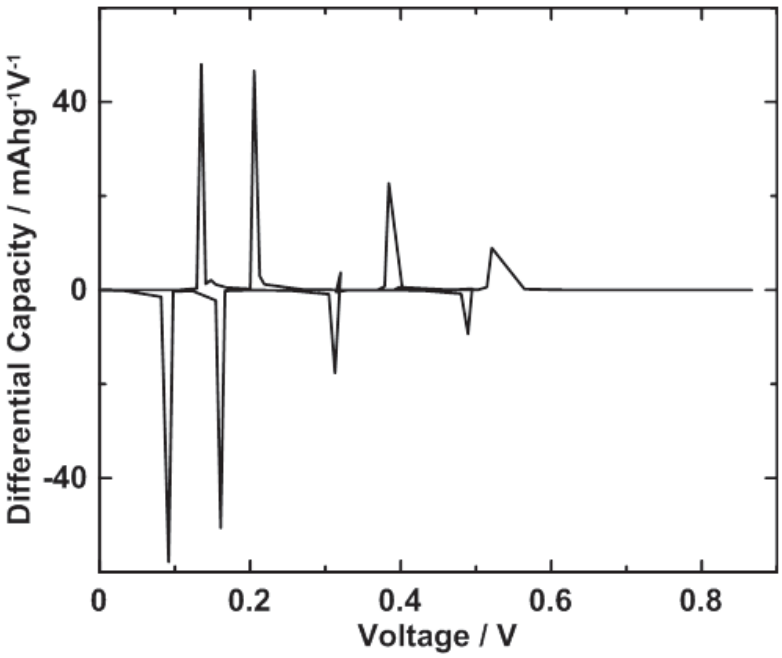

Figure 4.3.3: Differential capacity vs. voltage form Figure 4.3.1.

Figure 4.3.4 shows the in-situ XRD patterns of a lead electrode in a sodium half-cell and its corresponding voltage curve. The initial XRD pattern is shown in Figure 4.3.5. The peaks correspond to lead metal. As sodiation proceeds, a new phase appears,

with the disappearance of lead peaks, confirming two-phase behaviour. Figure 4.3.6 shows the XRD pattern of the cell at the end of the first plateau (Scan 3), which matches the calculated pattern for of $NaPb_3$ (labeled β in the phase diagram shown in Figure 4.3.2). By the end of the second plateau, peaks corresponding to NaPb had formed (Figure 4.3.7, Scan 9) at the expense of the $NaPb_3$ phase. At the end of the third plateau, Na_9Pb_4 peaks are formed (Figure 4.3.8, Scan 18), which disappear during the fourth plateau as peaks from $Na_{15}Pb_4$ emerge (Figure 4.3.9, Scan 29). This process is completely reversible during the subsequent desodiation. After the first two half-cycles the in-situ cell demonstrated AHVIC and ceased cycling.

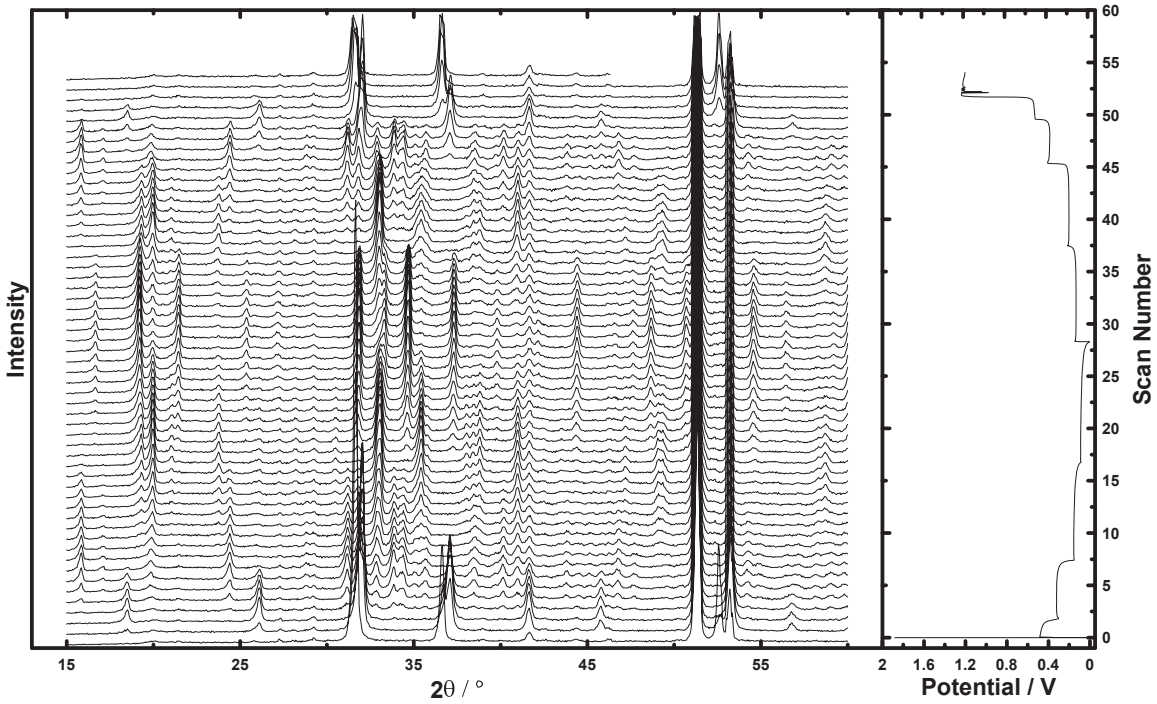

Figure 4.3.4: In-situ XRD measurements of the lead electrode during sodiation and subsequent desodiation, the cell voltage curve is shown vs. scan number to the left.

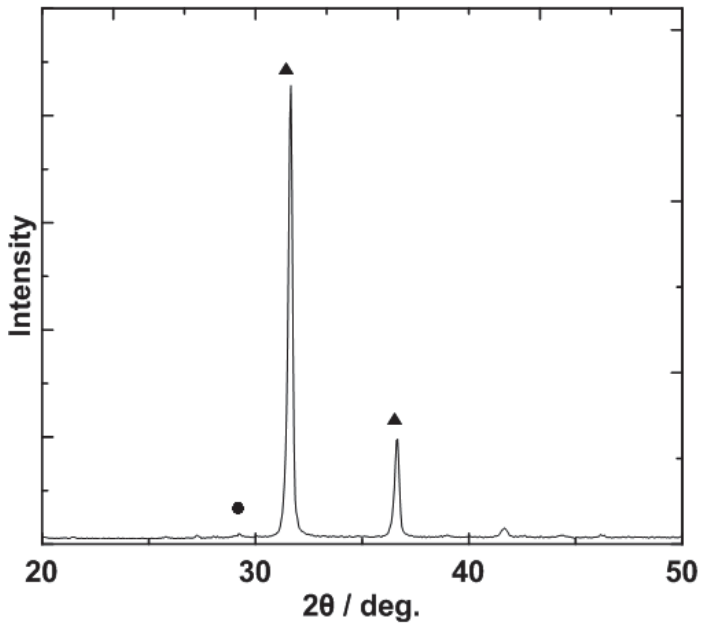

Figure 4.3.5: In-situ XRD pattern of lead before sodiation. Expected peak positions of lead are indicated by triangles. Peaks arising from beryllium and cell parts are labelled with dots.

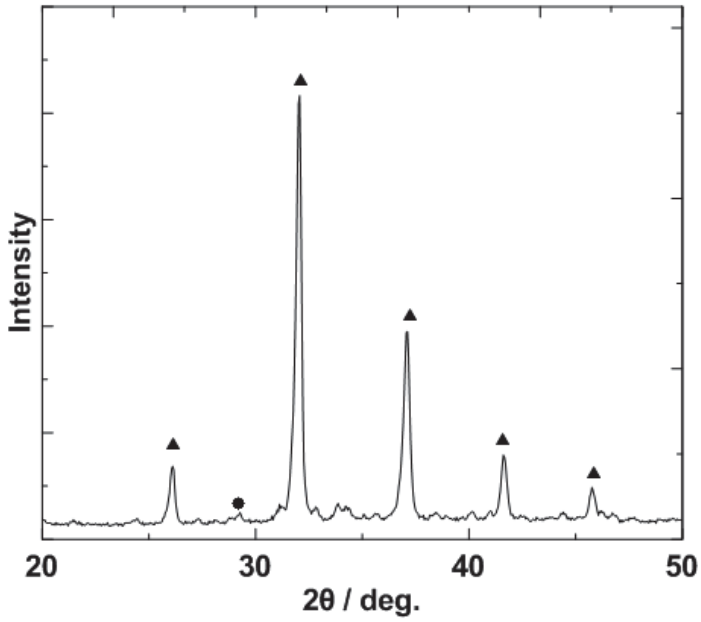

Figure 4.3.6: In-situ XRD pattern of the sodiated lead phase formed at the end of Plateau 1 (Scan 3). Expected peak positions of $NaPb_3$ are indicated by triangles. Peaks arising from beryllium and cell parts are labelled with dots.

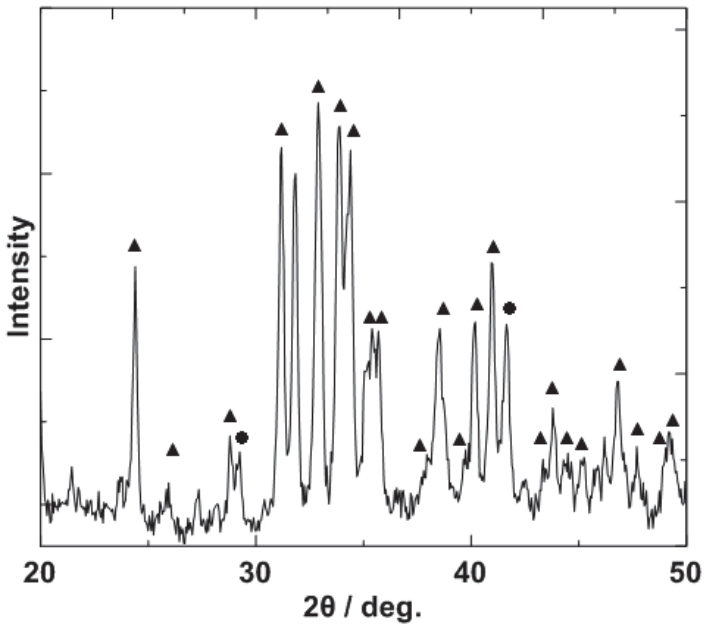

Figure 4.3.7: In-situ XRD pattern of the sodiated lead phase formed at the end of Plateau 2 (Scan 9). Expected peak positions of NaPb are indicated by triangles. Peaks arising from beryllium and cell parts are labelled with dots.

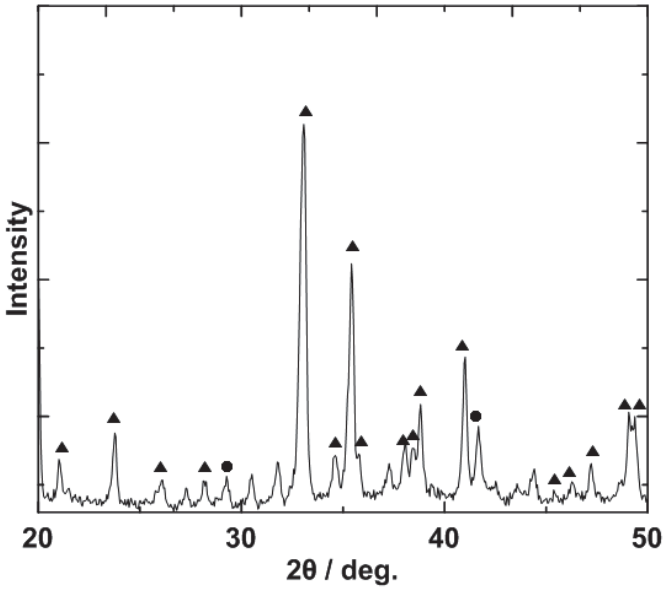

Figure 4.3.8: In-situ XRD pattern of the sodiated lead phase formed at the end of Plateau 3 (Scan 18). Peaks fit by Rietveld refinement discussed below are marked with triangles. Peaks arising from beryllium and cell parts are labelled with dots.

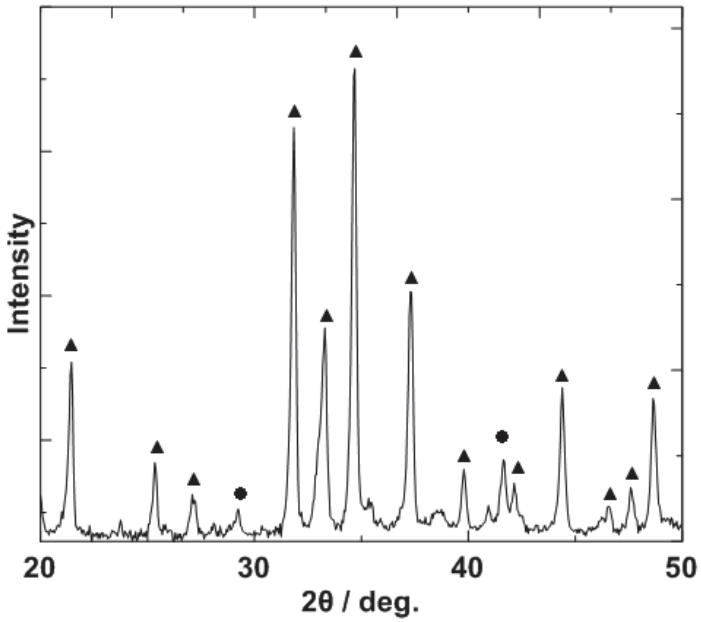

Figure 4.3.9: In-situ XRD pattern of the fully sodiated lead phase (Scan 29). Expected peak positions of $Na_{15}Pb_4$ are indicated by triangles. Peaks arising from beryllium and cell parts are labelled with dots.

Only incomplete crystallographic data for Na_9Pb_4 has been previously reported [48]. However, the XRD pattern of Na_9Pb_4 in Figure 4.3.8 is very similar to the calculated pattern of Na_9Sn_4 from a previous study [46], shown in Figure 4.2.7. Therefore Na_9Pb_4 was assumed to have the same space group (Cmcm). A Rietveld refinement was used to fit the XRD pattern of Na_9Pb_4 in Figure 4.3.8 using the space group and atom positions of Na_9Sn_4 [46]. Regions with cell part peaks were excluded from the refinement. The results of the refinement are listed in Table 4.3.1 and shown in Figure 4.3.10. The lattice parameters were found to be a=5.47, b=9.45, c=30.35 Å. A Bragg R factor of 5.52 was obtained. The small size of the sample, which was smaller than the x-ray beam width at low angles, cell component peaks and Be window peaks contributed to the large value of R. The space group and lattice constants found by this

refinement are still accurate however. Minor peaks that do not agree with this fit may be from the formation of $Na_5Pb_{2.}$, which is stochiometrically close to Na_9Pb_4, however crystallographic information for this phase has not been reported.

Table 4.3.1: Parameters obtained from the Rietveld refinement of scan 17, $Na_9Pb_{4,}$ to Na_9Sn_4 [46].

Phase			Na_9Pb_4	
Space Group			Cmcm	
Z			4	
a /Å			5.47(1)	
b /Å			9.45(0)	
c /Å			30.35(6)	
Bragg R.			5.52	
Atom	**Site**	**x**	**y**	**z**
Pb_1	8f	0	0.81(1)	0.79(8)
Pb_2	8f	0	0.49(9)	0.950(6)
Na_1	8f	0	0.8(8)	0.57(5)
Na_2	8f	0	0.3(8)	0.85(7)
Na_3	8f	0	0.8(7)	0.34(7)
Na_4	8f	0	0.8(2)	0.51(7)
Na_5	4c	0	0.8(1)	0.25

As shown in Figures 4.3.1 and 4.3.4, the lead half-cells presented here do not operate after more than a single cycle due to AHVIC. The report by Jow et al. does not mention any sign of AHVIC and shows 180 cycles with 80% capacity retention for lead-composite electrodes cycled vs. sodium metal in a beaker-type cell [9]. The half-cells that Jow et al. used were assembled in a charged state, with sodium metal already alloyed in the lead. Jow et al. had no need therefore to apply a high current pulse prior to cycling, as was necessary here, since the catalytic decomposition of electrolyte on clean unsodiated lead would not occur. Additionally, cells cycled multiple times by Jow et al. had an upper voltage limit of 0.45 V. This limited cycling of the electrode to the lower

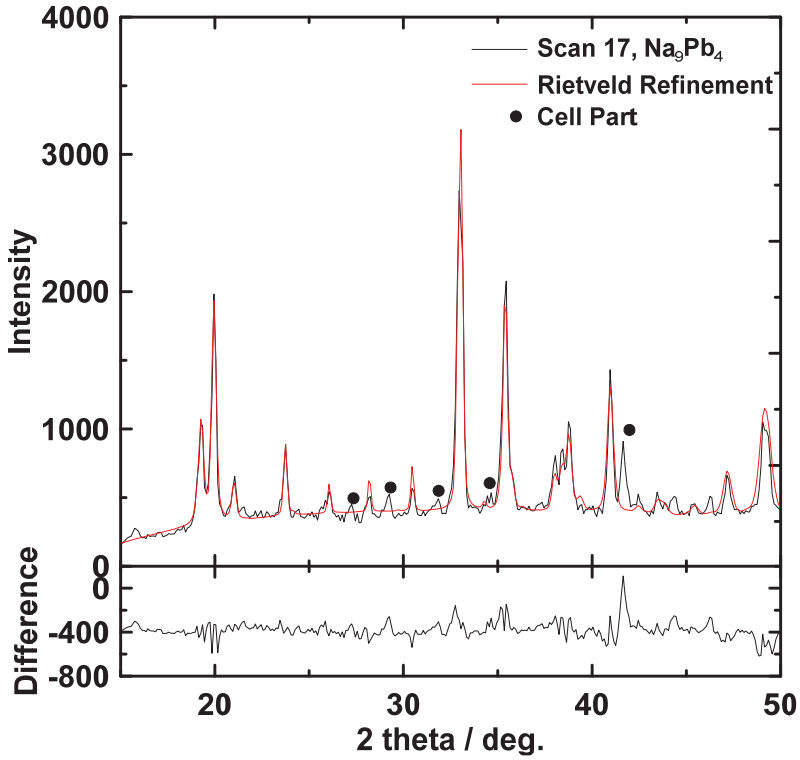

Figure 4.3.10: In-situ XRD pattern of the sodiated lead phase formed at the end of Plateau 3 (Scan 18) in black and the fit from the Rietveld refinement in red. Below in black is the difference between experimental and calculated paterns.

three voltage plateaus. Since the electrodes in their study were never fully desodiated, the effect of AHVIC was never observed. Jow et al. do show a complete voltage curve with all four plateaus for sodiation and desodiation, but only one cycle is shown.

Lead-polymide electrodes were made to test whether the cycling of lead electrodes could be improved by using a composite and by limiting the upper voltage, as shown by Jow. Additionally the lead-polyimide cells were cycled to four different cut-off voltages so that cycle life of the electrode could be tested up to various states of charge. The voltage curve shown in Figure 4.3.1 shows a remarkably small hysteresis in the lower two plateaus, implying that the phase transitions occurring are fast and may not

involve significant structural change from the host. Large structural changes in a host material often result in large hysteresis, poor kinetics and the destruction of the electrode after multiple cycles, which can be observed by the capacity fade.

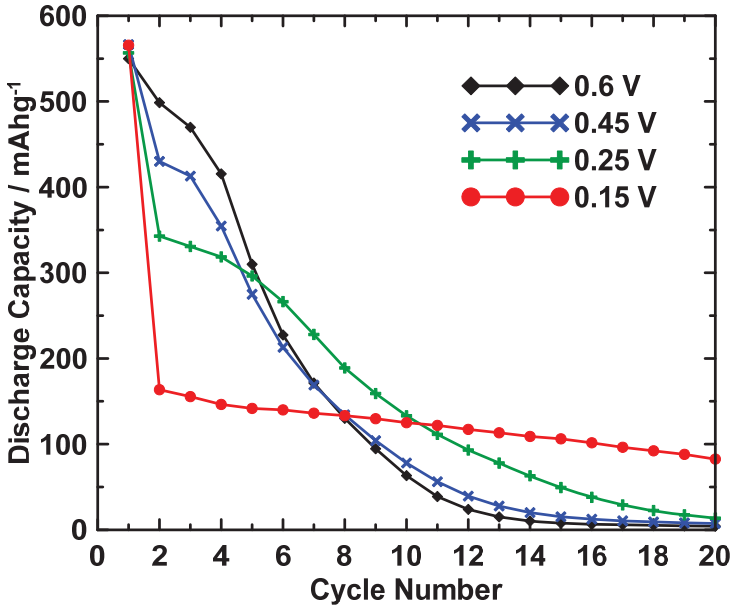

Figure 4.3.11: Discharge capacity vs. cycle number for lead-polymer half-cells charged to different voltage limits.

Figure 4.3.11 shows the capacity fade for the lead-polymer electrodes described above. Capacities higher than 485 mAh/g, theoretical capacity of lead, were observed. This is likely because polymide is irreversibly reacting with sodium, as it has been observed to do so with lithium [49]. An initial high current pulse was applied prior to cycling, however AHVIC was not observed in these cells at any time. It is possible that the polyimide binder protected the surface of the lead particles from catalytic activity. Figure 4.3.11 shows capacity fade and failure within 10 cycles when the cells are cycled on all four plateaus (to 0.6 V) or on the bottom three plateaus (to 0.45 V). Better cycling is

obtained when the cell is cycled on the bottom two plateaus (to 0.25 V). Good capacity retention over 20 cycles is obtained when the cell is cycled exclusively on the lowest plateau (to 0.15 V). This suggests that the phase transition between Na_9Pb_4 and $Na_{15}Pb_4$, (corresponding to the lowest plateau in the voltage curve as shown by in-situ XRD above) may be infliciting little stress to the electrode material, as suggested by the low hysteresis.

4.3.4 Conclusion

The discharge capacity of lead was found to be 317 mAh/g, which approaches the theoretical capacity for $Na_{15}Pb_4$. The lead vs. sodium voltage curve shows four main plateaus, corresponding to the phases: $NaPb_3$, NaPb, Na_9Pb_4 and $Na_{15}Pb_4$. The presence of these four phases was confirmed by in-situ XRD. The Na_5Pb_2 phase may also have been formed, indicated by a small plateau that was observed only during the desodiation half-cycle, but little evidence of this phase was observed by XRD. AHVIC occurred whenever pure lead was formed. This effect has up until now been only observed with tin electrodes. As with tin, a high current pulse was successful for inducing proper cycling. Lead-polyimide composite electrodes were less likely to demonstrate AHVIC. It is suspected that the metal surface was protected by the polymer coating. Lead-polymer cells cycled on the lower two voltage plateaus retained their capacity better than cells cycled over the entire voltage range. The lower plateaus also have low hysteresis. It is suspected that the phase transitions between NaPb, Na_9Pb_4 and $Na_{15}Pb_4$, (occurring on the lower two plateaus), induce less stress on the electrode material, allowing for longer cycle life.

4.4 Sodium Insertion into Bismuth

4.4.1 Introduction

Lithium insertion in bismuth has an average voltage of about 0.8 V vs Li, which makes it less attractive than other elements that alloy with lithium at lower voltages, such as silicon or tin [50]. Studies of bismuth electrodes in lithium cells have found that the lithiation of bismuth follows the Li-Bi equilibrium phase diagram, with the formation of BiLi and $BiLi_3$ [50]. Bismuth could be a more attractive anode candidate for sodium-ion batteries, since from electronegativity differences one would predict that the voltage of Bi vs. Na should be lower than the voltage of Bi vs. Li. According to the equilibrium binary phase diagram for the Na-Bi system, BiNa and $BiNa_3$ are the only thermodynamically stable Na-Bi phases at ambient temperatures. The Na-Bi system bears much resemblance to the phase diagram of Li-Bi [25]. A previous study of the open-circuit potential of a Na-Bi cell at 586^0C reported that 55 mole% sodium could be inserted into bismuth at full sodiation [51]. The electrochemical insertion of sodium into bismuth at room temperature has not been previously reported.

4.4.2 Experimental

Sputtered bismuth electrodes were made and tested as described in Section 4.0.2. In-situ XRD cells were made as tested as described in Section 2.33 and Table 4.0.1.

4.4.3 Results and Discussion

Figure 4.4.1 shows the voltage curve for the first 1.5 cycles of a bismuth half-cell. AHVIC was not observed during the sodiation of bismuth. During each half-cycle, two

plateaus of constant voltage are observed, corresponding to two two-phase regions. A capacity of 378 mAh/g was obtained during the first discharge, which is near the theoretical capacity of bismuth (385 mAh/g, assuming the most sodiated Na-Bi phase, $BiNa_3$, is formed). The average voltage, as measured from during the first desodiation half-cycle and the subsequent sodiation half-cycle, is 0.6 V, which is less than the average voltage of a Bi vs. Li cell (0.8 V), as expected. Figure 4.4.2 shows the voltage curve of the first sodiation of bismuth plotted vs. atomic percent sodium, and overlaid onto the Na-Bi binary alloy phase diagram [25]. The plateaus in the voltage curve closely match with the two-phase regions in the phase diagram, suggesting that the equilibrium phases are formed during cycling.

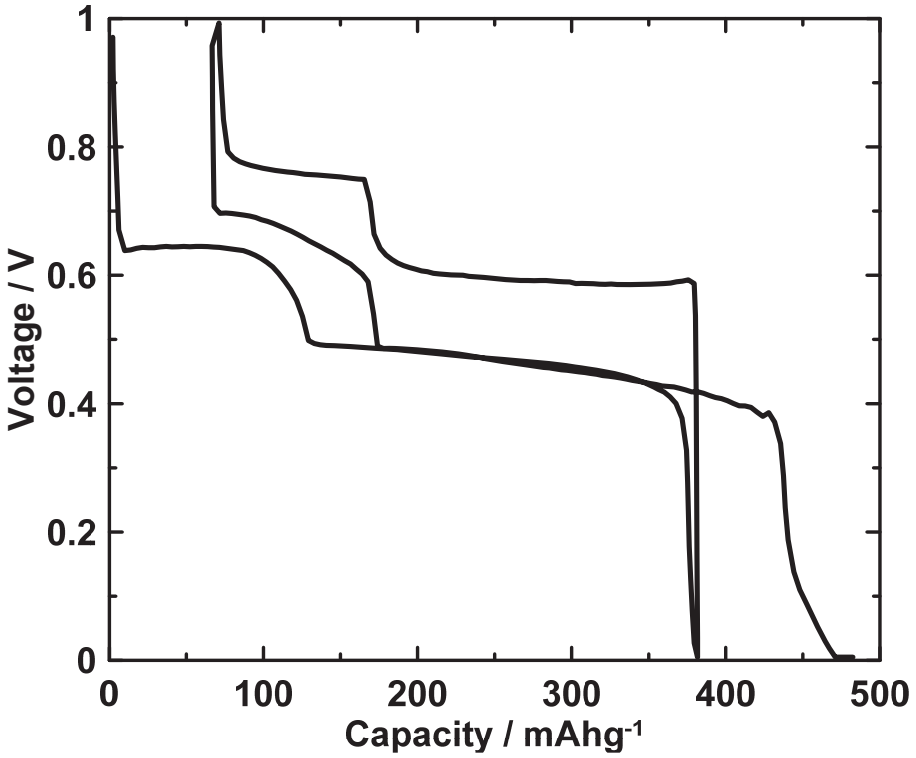

Figure 4.4.1: Voltage curve displaying reversible insertion of sodium into sputtered bismuth.

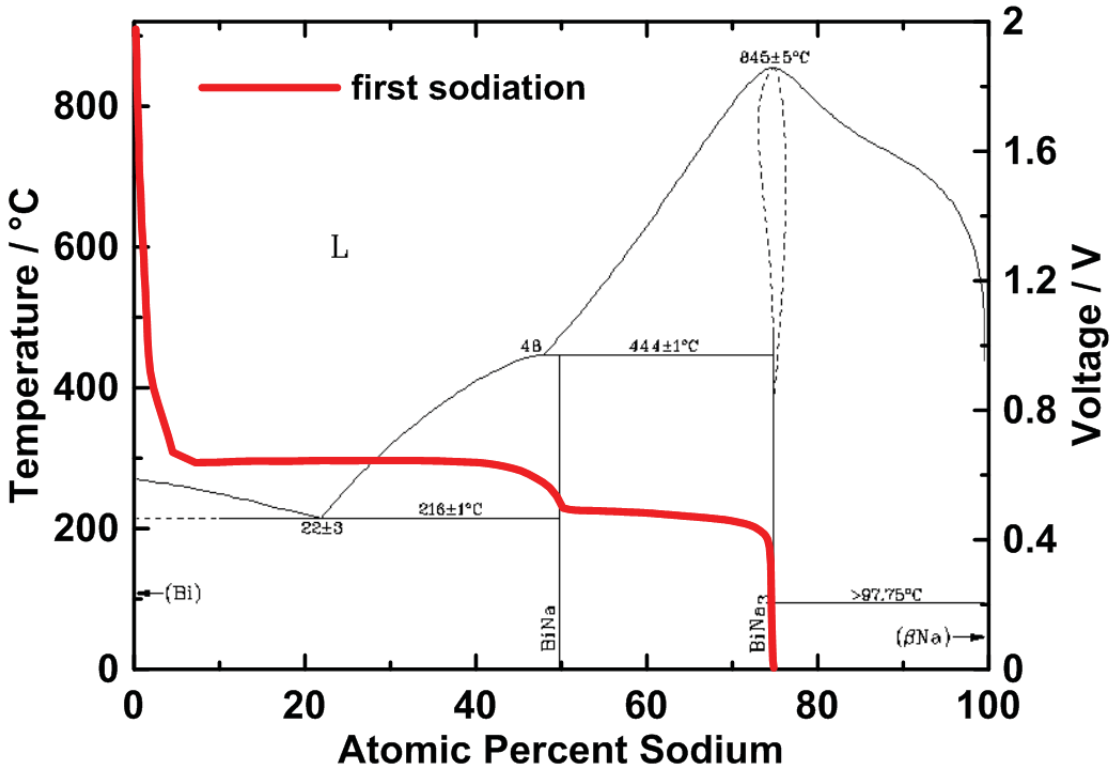

Figure 4.4.2: Voltage curve of the first sodiation half-cycle of sputtered bismuth overlaid onto the Na-Bi binary phase diagram [25].

In-situ XRD patterns of a sputtered bismuth electrode in a Bi vs. Na cell, and the corresponding cell voltage curve, are shown in Figure 4.4.3. The XRD pattern of the cell prior to cycling is shown in Figure 4.4.4. The peaks marked with triangles correspond to bismuth metal and the peaks marked with circles are from cell parts. As sodiation continued, the appearance of a new phase, with the disappearance of bismuth peaks confirmed two-phase behaviour.

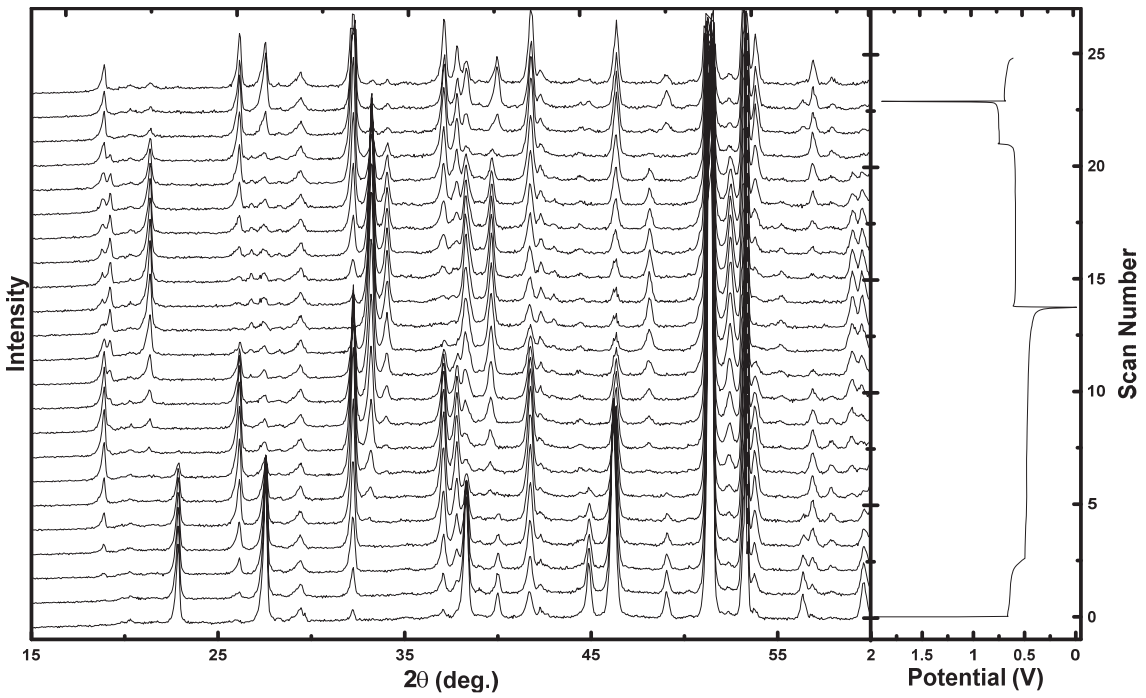

Figure 4.4.3: In-situ XRD measurements of the bismuth electrode during sodiation and subsequent desodiation, and the corresponding voltage curve.

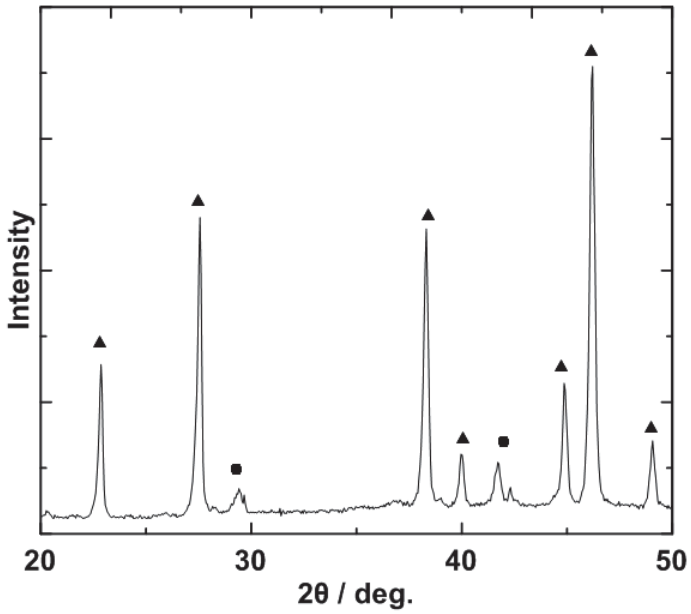

Figure 4.4.4: In-situ XRD pattern of bismuth before sodiation (Scan 1). Expected peak positions of Bi are indicated by triangles (▲). Peaks arising from beryllium and cell parts are labelled with dots (●).

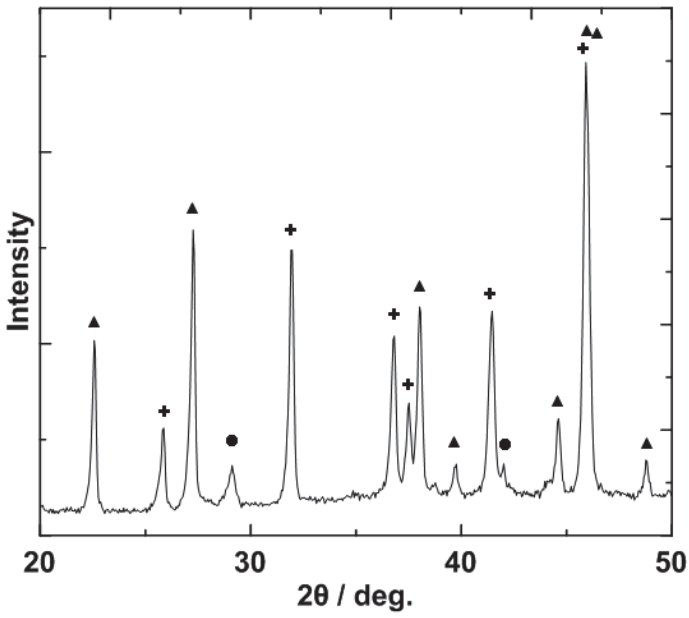

Figure 4.4.5: In-situ XRD pattern of the sodiated bismuth phase formed during Scan 4. Expected peak positions of BiNa and Bi are indicated by crosses (✚) and triangles (▲), respectively. Peaks arising from beryllium and cell parts are labelled with dots (●).

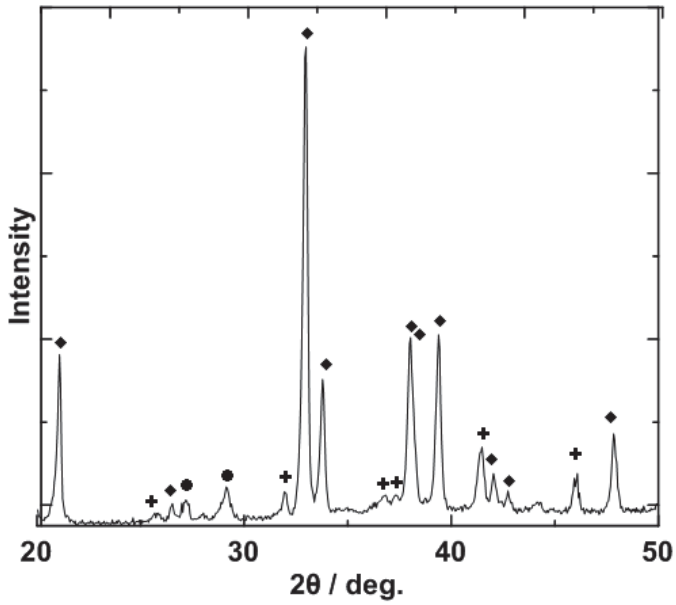

Figure 4.4.6: In-situ XRD pattern of the sodiated bismuth phase formed during Scan 15. Expected peak positions of BiNa and $BiNa_3$ are indicated by crosses (✚) and diamonds (◆), respectively. Peaks arising from beryllium and cell parts are labelled with dots (●).

Figure 4.4.5 shows the XRD pattern of the cell near the end of the high voltage plateau (Scan 4). Peaks in the XRD pattern are consistent with the formation of BiNa. During the low voltage plateau, peaks from $BiNa_3$ formed (Figure 4.4.6) at the expense of the NaBi phase. This process is completely reversible during the subsequent desodiation.

4.4.4 Conclusion

The formation of $NaBi_3$ corresponds to a capacity of 385 mAh/g and 1075 mAh/cm^3, with 250% volume expansion of the alloy at full sodiation. Sodiation of bismuth to a final phase of $NaBi_3$, as predicted by the phase diagram, was confirmed by in-situ XRD. The gravimetric sodiation capacity of this material is higher than that of hard carbon, and is comparable to the lithiation capacity of graphite. The volumetric energy density of $BiNa_3$ roughly double that of hard carbon, making it an interesting candidate for a sodium-ion anode material.

CHAPTER 5 SODIUM INSERTION INTO A TIN-COBALT-CARBON ACTIVE/INACTIVE NANOCOMPOSITE

5.1 Introduction

It was shown in Section 4.2 that the sodiation of tin results in the formation of $Na_{15}Sn_4$, corresponding to a capacity of 847 mAh/g or 1177 Ah/L . This far exceeds the capacity of hard carbon or any other anode material used for sodium thus far. However, it is well known that the large volume changes during cycling of alloy materials leads to their degradation and early cell failure. One method of increasing cycle life of an alloy negative electrode is by incorporating an inactive material and forming a nanocomposite particle [20].

The Sn-Co-C alloy system has been extensively studied for use in Li-ion batteries. Such alloys have been described as CoSn alloy grains in a matrix of disordered carbon [52]. In 2005 Sony commercialized the Nexelion™ litium-ion battery, which contains an active/inactive anode composed of a tin-cobalt alloy in a carbon matrix [53]. The Dahn group studied the Sn-Co-C system using samples made by sputtering and ball milling [52,54-56]. In particular, the $Sn_{0.3}Co_{0.3}C_{0.4}$ composition was extensively studied. This composition has a theoretical capacity of 701 mAh/g vs. lithium, based on the reaction of 4.4 Li per atom of tin and 0.5 Li per atom of carbon, however the capacities of materials prepared by ball milling could only achieve two thirds of this capacity [53]. It is thought that this is because some of the the tin within large CoSn grains in ball milled materials is

inaccessible to lithium. The full theoretical capacity of $Sn_{0.3}Co_{0.3}C_{0.4}$ has only been approached through combinatorial sputtering, in which the grain sizes achieved are five times smaller than what can be obtained by mechanical means [55,56]

Here $(Sn_{0.5}Co_{0.5})_{1-x}C_x$ made by mechanically milling is studied as an anode material in a sodium-ion cell. This is the first reported study of an active/inactive alloy anode material for sodium cells. Mechanically milled $(Sn_{0.5}Co_{0.5})_{1-x}C_x$ materials were found to have significantly improved cycling compared to pure tin anodes. However the fraction of the theoretical capacity that is obtained is much lower than for the insertion of lithium in $(Sn_{0.5}Co_{0.5})_{1-x}C_x$ at the same temperature. By varying the amount of carbon in $(Sn_{0.5}Co_{0.5})_{1-x}C_x$ it was found that at 30°C only 8% of the tin is accessible for sodium insertion. The amount of accessible tin increases to 38% at 60°C. This suggests that the kinetics for sodiation are slow compared to lithiation of the same material.

5.2 Experimental

Sample Preparation

$(Sn_{0.5}Co_{0.5})_{1-x}C_x$ samples were were made by Dr. Pierre Ferguson and his summer student Miléna Martine [57] by ball milling stoichiometric amounts of $CoSn_2$, Co (Sigma-Aldrich®, < 150 μm, 99.9 +%), and graphite (Fluka, purum) in an argon atmosphere for 10 days. Hard carbon was made by ball milling graphite under the same conditions as $(Sn_{0.5}Co_{0.5})_{1-x}C_x$. Since ball milled carbons are air-sensitive, and in some cases pyrophoric, the ball milled carbon was then sealed under argon in a quartz tube and heated to 200° C under vacuum for two hours, which rendered it air-stable.

X-Ray Diffraction

XRD patterns of $(Sn_{0.5}Co_{0.5})_{1-x}C_x$ samples were measured with a JD2000 from 10-70 degrees 2-theta, with 0.05 degrees per step, and a 10 second count time.

XRD patterns of the air-sensitive ball milled hard carbon were measured under flowing helium in the air-tight sample holder shown in Figure 2.3.1. A Siemens D500 with a 0.15° receiving slit was used. Measurements were taken from 15-55 degrees two-theta, with 0.05 degrees per step, and a 10 second count time. The resulting data was corrected for the atomic form factor and the Lorentz-polarization factors to account for peak broadening at low angles, as described in Section 2.1 and reference [28].

Electrode preparation

$(Sn_{0.5}Co_{0.5})_{1-x}C_x$ electrodes were made by combining the active powder in a slurry with polyacrylic acid (35% solution in water, Aldrich®) in a 90:10 weight ratio. Deionized water was added to give the slurry a proper viscosity for coating. The slurry was mixed for one hour in a Retsch® PM200 planetary mill at 120 rpm with two tungsten carbide balls. The slurry was then coated using a doctor blade with a 0.002" gap onto copper foil and air dried in a convection oven at 90 °C for 4 hours.

Hard carbon electrodes were made by combining the annealed carbon in a slurry with Super P carbon black (MMM Carbon, Belgium) and PVDF binder (HSV 900, Kynar®) in a 80:12:8 weight ratio, with NMP (>99.5%, Aldrich®) added for proper viscosity. The slurry was mixed for one hour in a Retsch® PM200planetary mill at 120

rpm with two tungsten carbide balls, coated using a doctor blade with a 0.006" gap onto copper foil, and air dried in a convection oven at 120°C.

Electrochemical Testing

Electrodes 1.3 cm^2 in area, and having a theoretical capacity of about 1 mAh/cm^2, were punched from the coated foils described above. The electrodes were incorporated as working electrodes in coin cells, as described in Section 3.3.

Coin cells were cycled, between 5 mV and 1.2 V at a rate of C/25 in a thermostatically controlled chamber at either 30°C or 60°C. After full sodiation was achieved, the cells were held at a constant potential of 5 mV until the current decreased to C/50.

5.3 Results and Discussion

The diffraction patterns of ball milled hard carbon before and after annealing at 200°C are shown in Figure 5.1. Two broad peaks at 25° and 44°can be attributed to regions of graphitic crystallites in the hard carbon matrix and correspond to reflections from the 002 and 100 planes in graphite [28]. The peaks are broadened due to the disordered nature of hard carbon and their small crystallite size [28]. The x-ray patterns were corrected for the carbon atomic form factor and the LPF, as described in Section 2.1, and fit with pseudo-Voigt peak profiles and a quadratic background function using a least squares fitting routine. By applying the Scherrer Equation 2.12, to the corrected peak widths, it was found that the average height and lateral extent of the graphite crystallites (L_c and L_a, respectively) increased after heat treatment at 200°C: L_a increased from 21 Å to 23 Å, while L_c increased from 10 Å to 12 Å. This is in accordance with the

'falling cards' model for disordered carbons, in which graphene sheets are expected to 'fall' and reorient in parallel with other graphene sheets as heating temperature is increased [15].

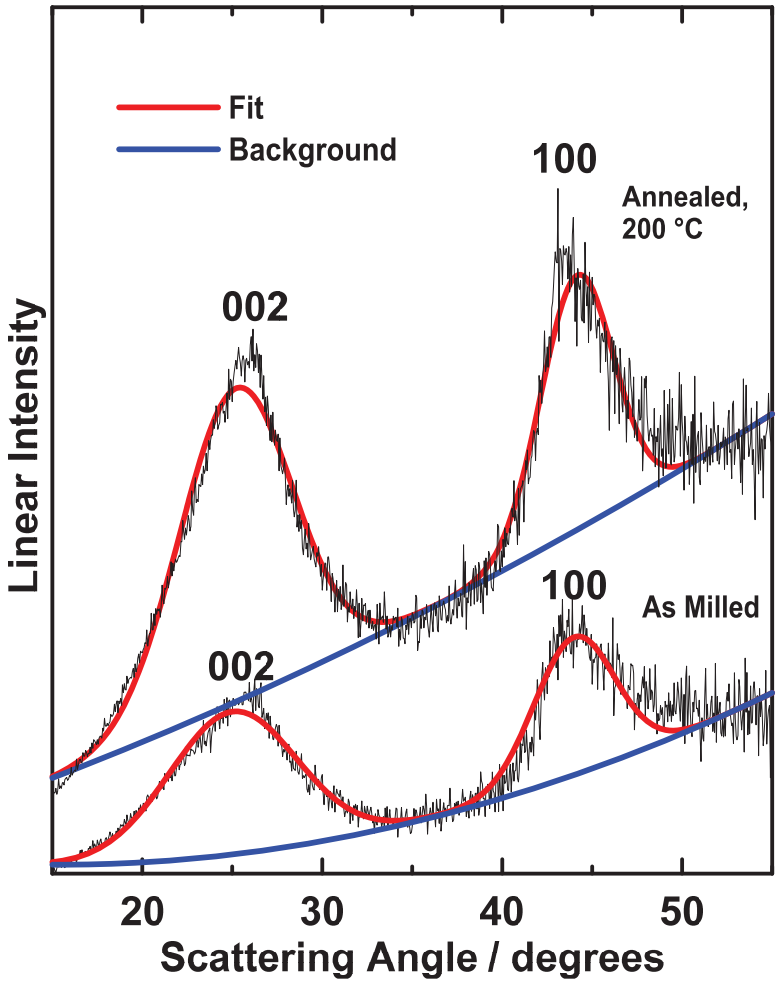

Figure 5.1: XRD patterns of ball milled hard carbon as milled and after heat treatment.

Figure 5.2 shows the voltage curve from ball milled hard carbon. During the first sodiation a large capacity is obtained of about 650 mAh/g and 910 mAh/g at 30°C and 60°C, respectively. However, subsequent cycling results in a featureless voltage curve with about 130 mAh/g reversible capacity between 5 mV and 1.2 V at both temperatures

(corresponding to the insertion of 0.058 Na per formula unit of carbon). The voltage curves consist only of a sloping voltage region and lack the characteristic low voltage plateau of hard carbon derived from pyrolysis, shown in Figures 2.1.1 and 3.2. This indicates that ball milled hard carbon lacks the nanoporous framework that accommodates sodium clusters. Minimal capacity fade was seen over the 10 cycles for which the cells were tested.

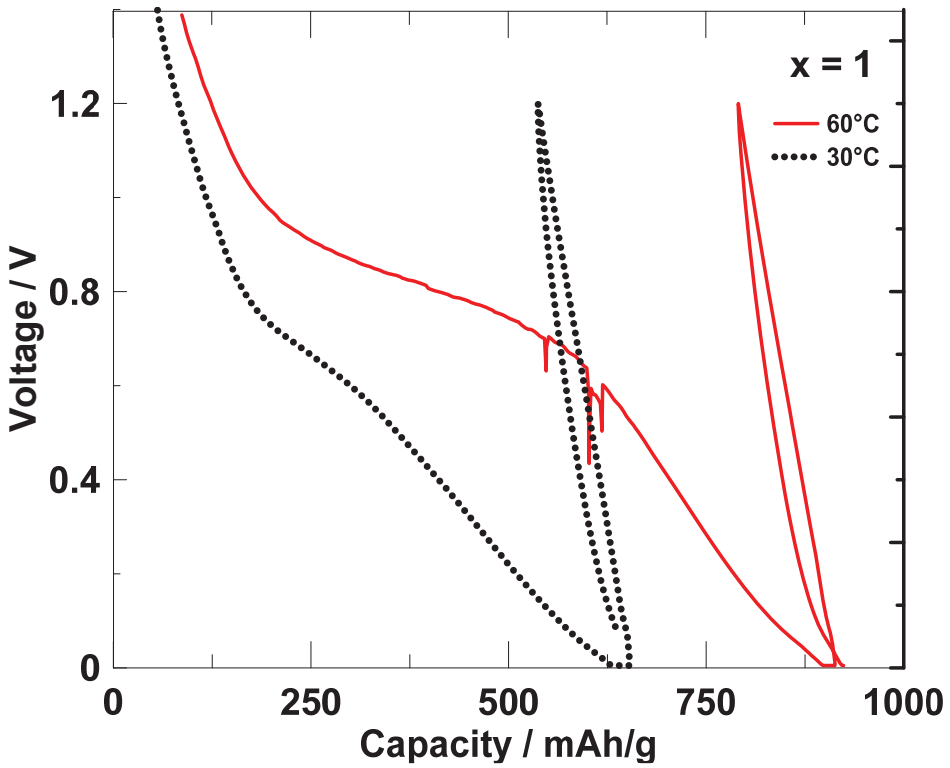

Figure 5.2: Voltage curves for ball milled, heat treated hard carbon at 30 °C in black, and at 60 °C in red.

The irreversible capacity of the ball milled hard carbon is much larger than that for hard carbons produced by pyrolysis, which is typically about 100 mAh/g [58]. It is possible that the ball milled hard carbon has a much larger surface area, leading to its high irreversible capacity. As is evident in Figure 5.2, the irreversible capacity increases

with temperatures as parasitic reactions and SEI formation also become more severe at higher temperatures.

Figure 5.3 shows the XRD patterns for $(Sn_{0.5}Co_{0.5})_{1-x}C_x$, $0.2 \leq x \leq 0.6$. The patterns show two broad peaks at 30° and 45°. These two peaks are characteristic to amorphous or nanostructured SnCo alloy in $(Sn_{0.5}Co_{0.5})_{1-x}C_x$ [54]. A small peak around 36° indicates a small amount of unreacted $SnCo_2$ starting material [55].

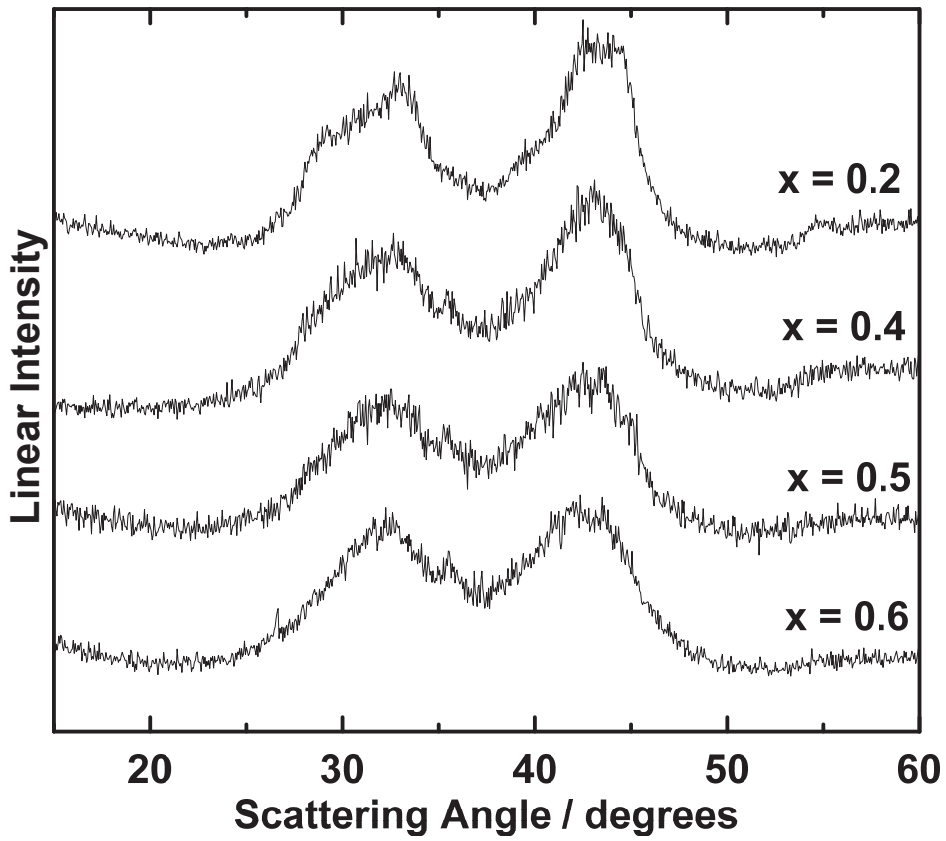

Figure 5.3: XRD patterns for ball milled $(Sn_{0.5}Co_{0.5})_{1-x}C_x$.

The voltage curves of $(Sn_{0.5}Co_{0.5})_{1-x}C_x$ vs. sodium metal at 30° and 60° C are shown in Figure 5.4. The theoretical capacity for each composition is also shown in Figure 5.4. To calculate the theoretical capacity it was assumed that sodium inserts into

tin to form the fully sodiated phase of $Na_{15}Sn_4$ and the capacity of the ball milled carbon in the alloy is 130 mAh/g, as shown in Figure 5.2 . At 30°C the reversible capacities at all values of x are much smaller than the theoretical capacity. At 60°C the reversible capacities are significantly increased, although they remain a fraction of the theoretical capacity and the capacity achieved by lithium insertion in alloys of the same composition[52]. This is evidence that the kinetics for sodiation of $(Sn_{0.5}Co_{0.5})_{1-x}C_x$ are much slower than for lithium.

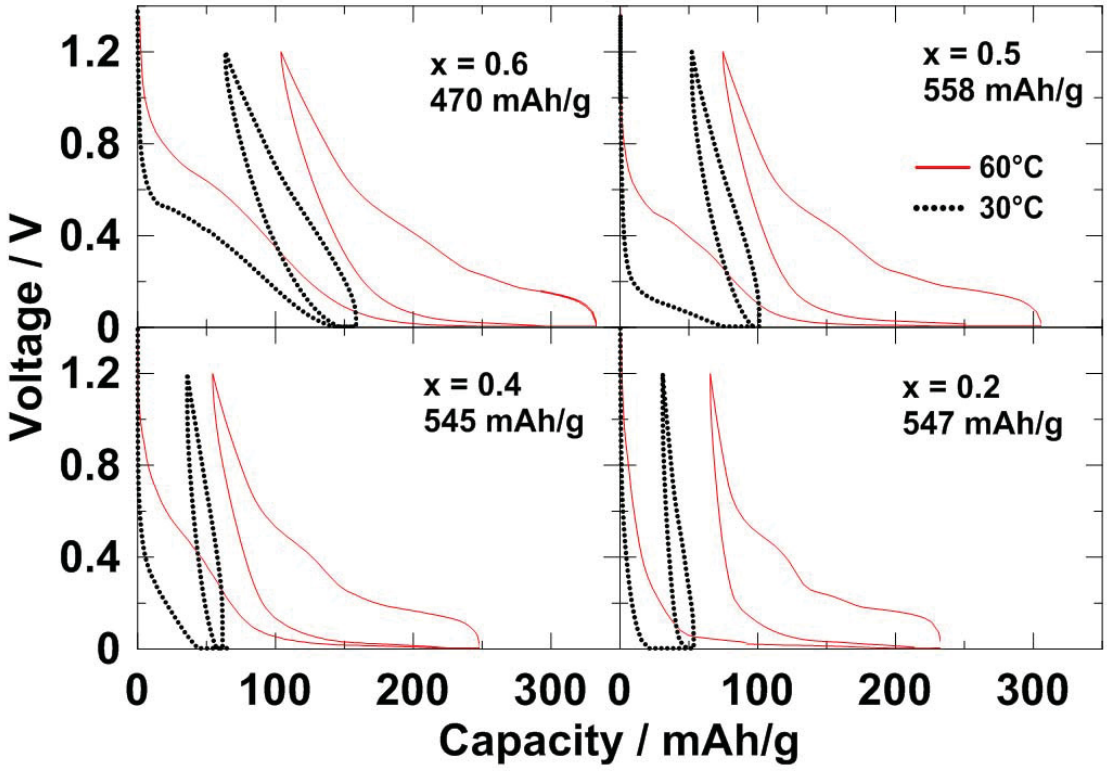

Figure 5.4: Voltage vs. capacity curves for $(Sn_{0.5}Co_{0.5})_{1-x}C_x$ in a sodium half-cell. Black dotted lines represent the voltage curves at 30 °C. Solid red lines represent the voltage curves at 60 °C.

Since ball milled Sn-Co-C alloys have lower than theoretical capacity due to the inability for lithium to access tin in the alloy, the same mechanism, acting at a greater extent, may also be causing the sodiation capacity to be low. To see if this is the case, the amount of sodium inserted reversibly into $(Sn_{0.5}Co_{0.5})_{1-x}C_x$ during the fourth charge/discharge cycle was calculated as y in $Na_y(Sn_{0.5}Co_{0.5})_{1-x}C_x$. Figure 5.5 shows a plot of y vs. x at 30°C and at 60°C. The relationship between y and x for both sets of data appear to be linear. This behaviour is consistent with a model that assumes all of the carbon in the alloy is accessible to sodiation, but only a fraction of the tin:

$$c = \left(a\,[3.75\,\tfrac{(1-x)}{2}] + 0.058x\right)\tfrac{F}{M} \qquad (5.1)$$

In this model, the sodium and carbon are assumed to have full sodiation capacities of 3.75 moles Na per Sn and 0.058 moles Na per C, a is the fraction of tin that is accessible in the alloy, c is the alloy capacity in mAh/g, x is the composition in $(Sn_{0.5}Co_{0.5})_{1-x}C_x$, M is molar mass of the alloy, and F is Faraday's constant (F = 26,802 mAh/mol). In Figure 5.5 solid lines show the theoretical capacity of the composites according to Equation 5.1 with a = 0.08 and 0.38 for 30°C and 60°C, respectively, as optimised by a least squares fitting routine. This model fits the data well with coefficient of determination (R^2) values of 0.99 and 0.92 for 30°C and 60 °C respectively. This indicates only a fraction of the tin is accessible for sodiation and that this fraction is independent of the carbon content, but is dependent on temperature. This is reasonable, since the amount of sodium that can be inserted in Sn-Co-C is likely related to the CoSn grain size, as is the case for the insertion of lithium. It has been shown that the grain size of $(Sn_{0.5}Co_{0.5})_{1-x}C_x$ does not change

appreciably with carbon content within the range of $0.2 \leq x \leq 1$ [53], thus the percentage of accessible tin remains constant in the $(Sn_{0.5}Co_{0.5})_{1-x}C_x$ series.

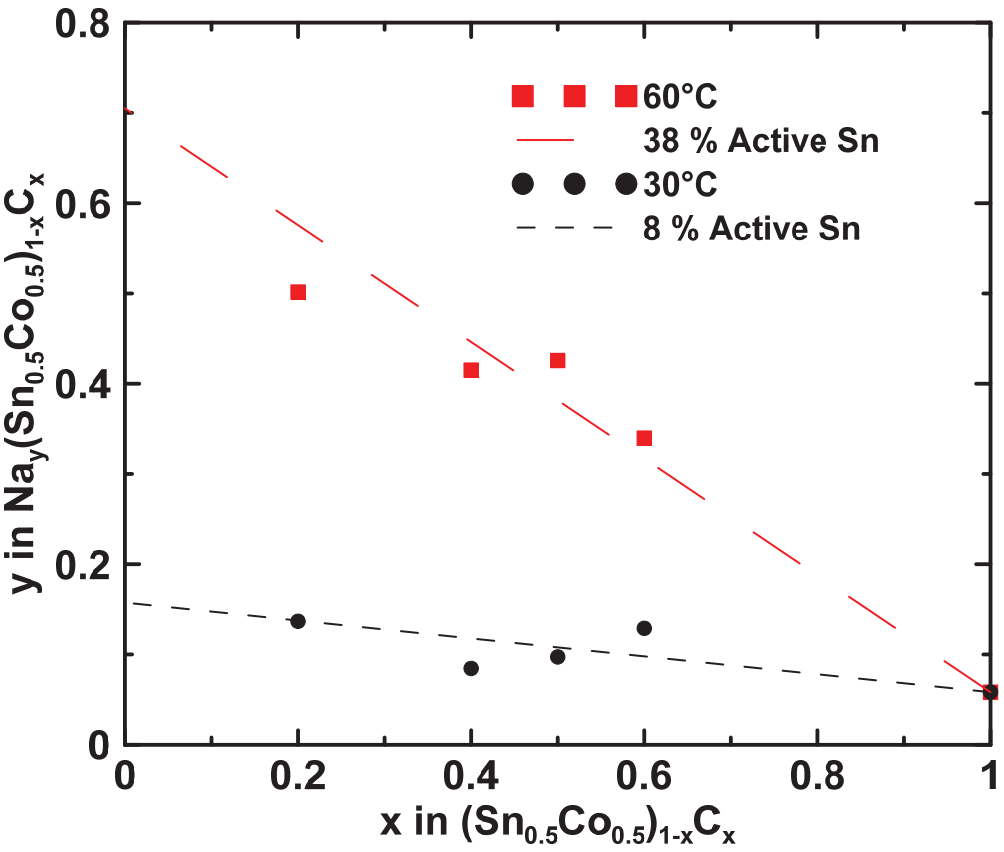

Figure 5.5: Number of sodium atoms inserted into $(Sn_{0.5}Co_{0.5})_{1-x}C_x$ vs. x. Black dots are experimental data points at 30 °C. The black dashed line represents a fit for these points using equation (5.2) with a = 0.08. Red squares are experimental data points at 60 °C. The red line represents a fit for these points using equation (5.1) with a = 0.38.

Figure 5.6 compares the cycling performance of sputtered tin to that of $Sn_{0.3}Co_{0.3}C_{0.4}$ alloy in sodium half-cells at 60°C and 30°C. As in the case of lithium cells, cycling performance is enhanced when an active/inactive alloy is used, however the capacity is greatly reduced in this case because the sodium is unable to access all the active tin. Nevertheless, using alloy volume expansion theory [24], the 200 mAh/g

reversible capacity observed here at 60°C corresponds to a volumetric capacity of 697 Ah/L with an alloy volume expansion of 86%. This is an equivalent volumetric capacity as graphite in a lithium ion cell and a volume expansion that can be accommodated in commercial cells. This is a much superior volumetric energy density than hard carbon. If capacities can be further increased at room temperature, such active/inactive alloys could be effective negative electrodes in sodium ion cells.

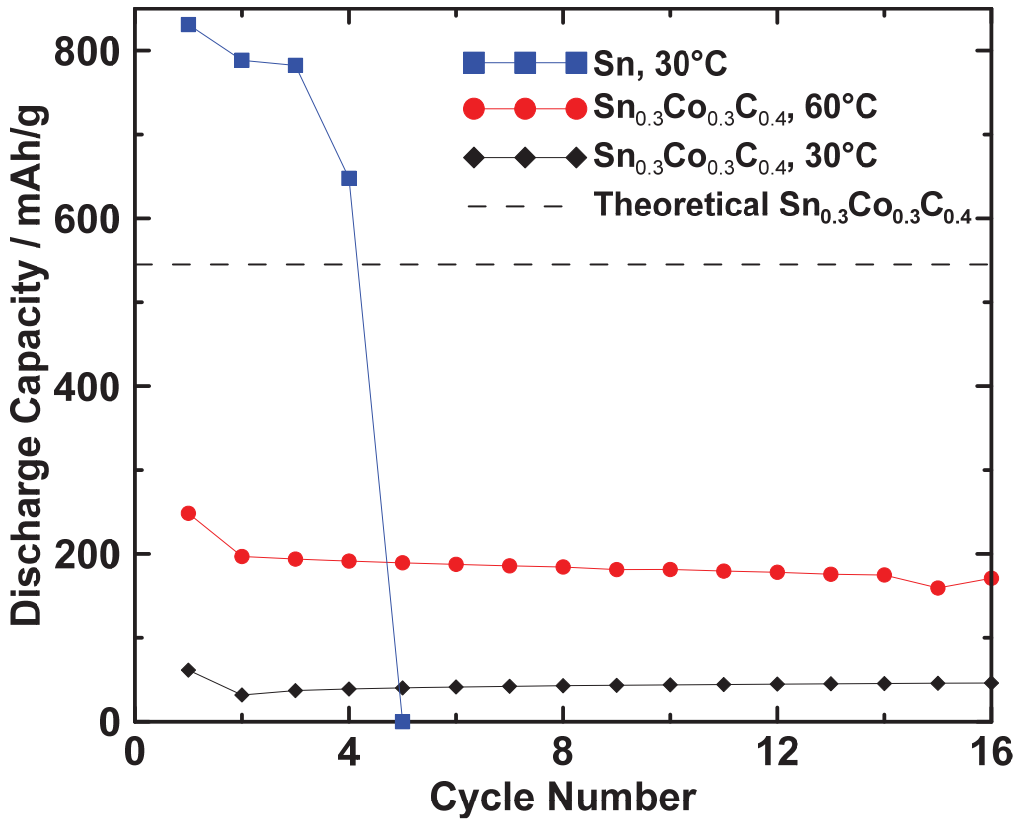

Figure 5.6: Capacity vs. cycle number for tin metal (blue squares) and $Sn_{0.3}Co_{0.3}C_{0.4}$ at 30 °C (black diamonds), and 60 °C (red circles).

5.4 Conclusion

Active/inactive $(Sn_{0.5}Co_{0.5})_{1-x}C_x$ alloy materials made by mechanical milling were cycled vs. a sodium anode. As with the lithiation of mechanically milled $(Sn_{0.5}Co_{0.5})_{1-x}C_x$, the full theoretical capacity was not achieved, presumably due to inaccessible tin embedded in the centre of large CoSn grains. The capacity of $(Sn_{0.5}Co_{0.5})_{1-x}C_x$ was seen to increase approximately seven fold when the temperature was raised from 30 °C to 60 °C. It was found that graphite milled under the same conditions as the $(Sn_{0.5}Co_{0.5})_{1-x}C_x$ formed a hard carbon, with a reversible capacity of 130 mAh/g. It was deduced that only 8 % of the tin in $(Sn_{0.5}Co_{0.5})_{1-x}C_x$ was accessible at 30°C, increasing to 38% at 60°C, with the rest of the capacity coming from the carbon matrix. Nevertheless at 60°C a reversible volumetric capacity equivalent to that of graphite in a lithium ion cell was obtained, with an associated volume expansion of 86%, which is reasonable for use in commercial cells. Further improvements are needed to increase the room temperature capacity of these materials.

CHAPTER 6 CONCLUSIONS

When this project started, little was known regarding the use of alloys for high capacity anode materials for sodium-ion batteries. The most widely studied sodium-ion anode material at the time was hard carbon, which has a capacity of 300 mAh/g and 630 mAh/cm^3 [14]. Based on known intermetallic phases, silicon, tin, lead and bismuth were thought to be interesting candidates for sodium-ion anode materials [25]. Sodium alloys with each of these elements have theoretical gravimetric capacities up to 900 mAh/g and volumetric capacities up to 900 mAh/cm^3.

Before investigating the properties of these alloy anode materials, it was necessary to optimise sodium half-cell construction (Chapter 3). A cell design using a combination of BMF and Celgard separators was developed that resulting in stable cycling for more than 35 cycles in sodium vs. hard carbon half-cells. This optimised coin cell construction is now a standard method of the Obrovac lab for sodium work, and enables all the electrochemical testing on sodium-ion materials done in this lab. Sodium cells used throughout the rest of this work were made by this method.

Silicon was predicted to form a fully sodiated phase of NaSi with a capacity of 954 mAh/g and 900 mAh/cm^3 , as discussed in Section 4.1. Only 200 mAh/g of capacity was obtained on the first discharge, and none on the subsequent cycles. The first discharge capacity could result from the formation of SEI on the sputtered electrode surface, although a small plateau at 0.4 V, close to the predicted voltage for sodiation, indicates that sodium insertion might be taking place. Poor kinetics might be the cause of

incomplete sodiation at room temperature. Further work on this system is needed to test this hypothesis.

The full sodiation of tin, Section 4.2, was expected to result in the formation of $Na_{15}Sn_4$, corresponding to 847 mAh/g and 1210 mAh/cm^3. AHVIC was observed in cells containing sputtered tin electrodes, and is thought to be caused by catalytic degradation of electrolyte on fresh metallic surfaces. An initial high current pulse was needed to initiate sodiation, which caused catalytic activity to be disrupted. The Na-Sn voltage curve had four plateaus, corresponding to four two-phase regions. The phase changes of tin upon sodiation were studied by in-situ XRD. Out of the four phases observed, two phases, $NaSn_3$ and Na_9Sn_4, had new crystalline structures which had not previously been seen in the literature, one phase, NaSn, was amorphous. The fully sodiated phase was found to be crystalline $Na_{15}Sn_4$, the thermodynamically stable phase at this composition. Further work needs to be done to characterise the crystal structures of the new phases. XRD patterns of better quality than the ones shown here are needed for structre determination of unknown phases. In-situ Mössbauer studies would be useful to complement the in-situ XRD work, and elucidate the chemical environment of tin atoms upon sodiation.

The full sodiation of lead, Section 4.3, was expected to result in the formation of $Na_{15}Pb_4$, corresponding to 485 mAh/g and 1182 mAh/cm^3. AHVIC was observed each time a current was applied to pure lead. It was found that if a high current pulse was applied, AHVIC could be completely eliminated. The voltage curve if sodium insertion in lead had four distinct plateaus, which aligned well with the sodium-lead binary phase

diagram. A Rietveld refinement of the Na_9Pb_4 phase with the crystallographic parameters of Na_9Sn_4 gave a good fit to the observed XRD pattern. A small fifth plateau observed only on desodiation indicates a fifth intermetallic phase is formed, likely Na_2Pb_5 , and that the sodiation and desodiation pathways are different. At full sodiation $Na_{15}Pb_4$ was observed, which is the thermodynamically stable phase at this composition.

The sodiation of bismuth, Section 4.4, was expected to result in the formation of $BiNa_3$ on full sodiation, corresponding to 385 mAh/g and 1075 mAh/cm^3. AHVIC was not observed in this system. The electrochemical sodiation of bismuth was confirmed by in-situ XRD to occur according to the binary phase diagram with BiNa and $BiNa_3$ being sequentially and reversibly formed.

The system with the highest capacity for sodium described above is tin. Sodium insertion into an optimised active/inactive nanocomposite based on $(Sn_{0.5}Co_{0.5})_{1-x}C_x$ was measured electrochemically over a range of x values (Chapter 5). It was found that the capacity obtained from these materials was much lower than the theoretical capacity. When the temperature of the reaction was increased from 30°C to 60°C the capacity improved, indicating that poor kinetics was the cause for incomplete sodiation. An empirical model was proposed in which the accessible amount of tin could be quantified. It was found by this model that only 8% of the tin could be sodiated at 30°C and 38% at 60°C. Stable cycling was observed for $Sn_{30}Co_{30}C_{40}$ over the 16 cycles that the cells were tested.

This thesis shows that sodium alloys could be used as high gravimetric and volumetric capacity sodium-ion anodes. Tin, lead and bismuth were shown to have

gravimetric and volumetric capacities that far exceeded hard carbon. AHVIC was shown to be problematic for the cycling of metallic tin and lead electrodes (Sections 4.2 ,4.3). AHVIC could be eliminated by applying a high current pulse prior to cycling, which formed a sodium alloy at the electrode surface, or by use of a polymeric binder or active/inactive composite, which modify the surface of metal particles. In-situ XRD on the tin and lead systems showed that upon sodiation crystalline phases with previously unreported structures were formed. Better quality XRD data should be obtained to characterise these phases further in order to fully understand the sodiation mechanisms. Poor sodiation kinetics for sodium insertion was observed with tin-cobalt-carbon and possibly with silicon, and limited the amount of capacity that could be obtained. Further work is needed to understand and improve sodiation kinetics of these materials in order to enhance their performance. The understanding of sodium insertion into metal anodes learned in this thesis is expected to contribute to the development of high capacity anode materials for practical sodium-ion batteries.

BIBLIOGRAPHY

[1] D. Linden, T.B. Reddy (Ed.), Ch. 26, Linden's Handbook of Batteries, 4th Edition. N ew York: McGraw-Hill, 2011.

[2] www.teslamotors.com.

[3] M.S. Whittingham, *Prog. Solid State Chem.*, **12**, 41 (1978).

[4] A.S. Nagelberg, W.L. Worrell, *J.Solid State Chem.*, **29**, 345 (1970).

[5] C. Delmas, J.J. Braconnier, C. Fouassier, P. Hagenmuller, *Solid State Ionics*, **4**, 165 (1981).

[6] J. Molenda, C. Delmas, P. Hagenmuller. *Solid State Ionics*, **10**, 431 (1983).

[7] L.W. Shacklette, T.R. Jow, L. Townsend. *J. Electrochem. Soc.*, **135**, 2669 (1985).

[8] J.M. Tarascon, G.W. Hull. *Solid State Ionics*; **22**, 85, (1986).

[9] T.R. Jow, L.W. Shacklette, M. Maxfield, D. Vernick, *J. Electrochem. Soc.,* **134**, 1730 (1987).

[10] K. West, B Zachau-Christiansen, T. Jacobsen, S. Skaarup. *Solid State Ionics*, **30**, 1128 (1988).

[11] S. Komaba, N.Yabuuchi, T.Nakayama, A. Ogata, T. Ishikawa, I.Nakai, *Inorg. Chem*., **51**, 6211(2012).

[12] X.Xia and J.R. Dahn, *Electrochem. Solid-State Lett.,* **15**, A11 (2012).

[13] D.P. DiVincenzo, E. J. Mele, *Phys. Rev. B.,* **32**, 2538, (1985).

[14] D.A. Stevens, J.R. Dahn, *J. Electrochem. Soc.,* **148**, A803, (2001).

[15] J.R. Dahn, W.Xing, and Y.Gao, *Carbon,* **35**, 825 (1997).

[16] Density of hard carbon: 2.11 ±0.01 g/cm^3, measured by helium pychnometry.

[17] M.N. Obrovac, L. Christensen, *Electrochem. Solid-State Lett.,* **7**, A93 (2004).

[18] 3M™ Battery Materials Brochure, 2011, http://multimedia.3m.com/mws/mediawebserver?mwsId=SSSSSufSevTsZxtUo8_B482GevUqevTSevTSevTSeSSSSSS--&fn=BatteryMaterials_6005400.pdf Accessed March 2013.

[19] M.N. Obrovac, L.J. Krause, *J. Electrochem. Soc.,* **154**, A103, (2007).

[20] O. Mao, B.L. Turner, D.W. McClure, I.A. Courtney, L.J. Krause, J R. Dahn, *Electrochem. Solid-State Lett.,* **2**, 3, (1999).

[21] L.W. Shacklette, T.R. Jow, L. Townsend, *J. Electrochem. Soc*., **135**, 2669. (1985).

[22] J. Li, D.B. Le, P.P Ferguson, J.R. Dahn, *Electrochimica Acta*, **55**, 2991, (2010).

[23] L.Y. Beaulieu, T.D. Hatchard, A. Bonakdarpour, M.D. Fleischauer, J.R. Dahn, *J.Electrochem. Soc.,* **150**, A1457 (2003).

[24] T.T. Tran, M.N. Obrovac, *J. Electrochem. Soc.,* **158**, A1411, (2011).

[25] Binary Alloy Phase Diagrams", ASM International (1996).

[26] R.D. Deslattes, E.G. Kessler, Jr., P. Indelicato, L. de Billy, E. Lindroth, J. Anton, *Rev. Mod. Phys*. **75**, 35, (2003).

[27] J. Biscoe, B.E. Warren, *J. Apl. Phys.* **13**, 364, (1942).

[28] J.R. Dahn, A.K. Sleigh, Hang Shi, B.M. Way, W.J. Weydanz, J.N. Reimers, Q. Zhong, U. von Sachen, Ch. 1, in: G. Pistoia (Ed.), Lithium Batteries – New Materials Developments and Perspective, Elsevier/North-Holland, 1993.

[29] D. Schaupp, M. Schumacher, F. Smend, P. Rullhusen, J.H. Hubbell, *J. Phys. Chem. Ref. Data,* **12**, 467 (1983).

[30] D.T. Cromer, J.T. Waber, *International Tables for X-Ray Crystallography*, Vol. IV, Ibers and Hamilton, eds (Kynoch Press, Birmingham, England, (1974), page 71

[31] "Lorentz-polarization correction" *Online Dictionary of Crystalography.* 2008. http://reference.iucr.org/dictionary/Lorentz%E2%80%93polarization_correction. Accessed March 2013.

[32] S. Komaba, W. Murata, I. Toru, N. Yabuuchi, T. Ozeki, T. Nakayama, A. Ogata, K. Gotoh, K. Fujiwara, Advanced Functional Materials, **21**, 3859 (2011).

[33] J. Sangster., A.D. Pelton., *J. Phase. Equilib.* **13**, 67, (1992).

[34] L.Monconduit, A. Darwiche, C. Marino, M.T. Sougrati, B. Fraisse, L. Stievano, *J. Am. Chem. Soc.,* **134**, 20805, (2012).

[35] J. Qian , Y. Chen , L. Wu , Y. Cao , X. Ai, H. Yang, *Chem Commun,* **48**, 7070, (2012).

[36] J. R. Dahn, S. Trussler, T. D. Hatchard, A. Bonakdarpour, J. R. Mueller-Neuhaus, K. C. Kewitt, M. Fleischauer, *Chem. Mater.,* **14**, 3519, (2002) .

[37] V. L. Chevrier, G. Ceder, J. Electrochem. Soc., **158**, A1011, (2011).

[38] I.A. Courtney, J.S. Tse, Ou Mao, J. Hafner, J.R. Dahn, *Phys. Rev. B.,* **58** , 15583, (1998).

[39] I.A. Courney, J.R. Dahn, *J. Electrochem. Soc.* **144**, 2045, (1997).

[40] J.R. Dahn, I.A. Courtney, Ou Mao, *Solid State Ionics*, **111**, 289, (1998).

[41] S. D. Beattie, T. Hatchard, A. Bonakdarpour, K. C. Hewitt, J. R. Dahn, *J. Electrochem. Soc.,* **150**, A701, (2003).

[42] R. Kremann, Julius Gmachl-Pammer, *Z. Metallk*, **12**, 257, (1920).

[43] W. Hume-Rothery, *J. Chem. Soc.,* **131**, 947, (1928).

[44] G. Deublein, H-C. Tsai, L. Z. Zhou, R. A. Huggins, *Solid State Ionics,* **42**, 109, (1990).

[45] S. Komaba, Y. Matsuura, T. Ishikawa, N. Yabuuchi, W. Murata, S. Kuze, *Electrochem. Commun*., **21**, 65, (2012).

[46] W. Müller, K. Volk,. *Z. Naturforsch*. **33**, 275, (1978).

[47] T. F. Faessler, C. Kronseder, *Angew. Chem. Int. ed.,* **37**, 1571, (1998).

[48] N. E. Weston, D. P. Shoemaker, Acta Crystallographica, **10**, 775 (1957).

[49] M.D. Fleischauer, M.N. Obrovac, J.R. Dahn, J. Electrochem. Soc., **155,** A851 (2008).

[50] W. Xianming, T. Nishina, I. Uchida, J. Power Sources, **104**, 90 (2002).

[51] Chemical Engineering Division Research Highlights, Argonne National Laboratory, 213 (1964).

[52] P.P. Ferguson, A.D.W. Todd, J.R. Dahn, *Electrochem Commun*, **10,** 25, (2008).

[53] http://www.sony.net/SonyInfo/News/Press/200502/05-006E/. Accessed July 2012.

[54] A.D.W. Todd, R.A. Dunlap, J.R. Dahn, *J. Alloys Comp*. 443, 114, (2007).

[55] A.D.W. Todd, P.P. Ferguson, M.D. Fleischauer, J.R. Dahn, *Int. J. Energ. Res.,* **34**, 535, (2010).

[56] A.D.W. Todd, P.P. Ferguson, J.G. Barker, M.D. Fleischauer, J.R. Dahn, *J. Electrochem. Soc.*, **156**, 12, (2009).

[57] P.P. Ferguson, Thesis (Ph.D.)--Dalhousie University (Canada), 2009

[58] F. Salver-Disma, C. Lenain, B. Beaudoin., L. Mymard, J.M. Tarascon, *Solid State Ionics*, **98**, 145, (1997).

APPENDIX

Request for Permission to Reproduce or Re-Publish ECS Material

Please fax this form to: The Electrochemical Society (ECS), Attn: Permissions Requests, 1.609.730.0629.
You may also e-mail your request to: copyright@electrochem.org. Include all the information as required on this form. Please allow 3-7 days for your request to be processed.

I am preparing a (choose one): ☐ paper ☐ chapter ☐ book ☒ thesis

entitled: Alloy Anodes for Sodium-Ion Batteries

to be published by: Library and Archives Canada

in an upcoming publication entitled:

I request permission to use the following material in the publication noted above, and request nonexclusive rights for all subsequent editions and in all foreign language translations for distribution throughout the world.

Description of material to be used—Indicate what material you wish to use (figures, tables, text, etc.) and give the full bibliographic reference for the source publication. You may attach a separate list, organized by ECS title.

Text and figures from:
1) Reversible Insertion of Sodium in Tin
L.D. Ellis, T.D. Hatchard, M.N. Obrovac, JECS, 159, (11), A1805, (2012)
2) Sodium Insertion into Tin Cobalt Carbon Active/Inactive Nanocomposite
L.D. Ellis, T.D. Hatchard, M.N. Obrovac, JECS, 160, A1, (2013)

Signature: [redacted] Date: April 4th 2013

Name: Leah Ellis

Address: Department of Chemistry, Dalhousie University
6274 Coburg Road,
P.O. box 15000
Halifax, N.S., B3H 4R2

Telephone: (902) 494-4060 Fax: (902) 494-1310

E-mail: leahellis@dal.ca

Permission is granted to reproduce the above-referenced material. Please acknowledge the author(s) and publication data of the original material, and include the words: "Reproduced by permission of The Electrochemical Society."

April 8, 2013
Date

[redacted]
Ann F. Goedkoop, Director of Publications